Understanding the Spatiotemporal Variability of Tropical Orographic Rainfall Using Convective Plume Buoyancy

QUENTIN NICOLAS[a] AND WILLIAM R. BOOS[a,b]

[a] *Department of Earth and Planetary Science, University of California, Berkeley, Berkeley, California*
[b] *Climate and Ecosystem Sciences Division, Lawrence Berkeley National Laboratory, Berkeley, California*

(Manuscript received 7 June 2023, in final form 20 December 2023, accepted 21 December 2023)

ABSTRACT: Mechanical forcing by orography affects precipitating convection across many tropical regions, but controls on the intensity and horizontal extent of the orographic precipitation peak and rain shadow remain poorly understood. A recent theory explains this control of precipitation as arising from modulation of lower-tropospheric temperature and moisture by orographic mechanical forcing, setting the distribution of convective rainfall by controlling parcel buoyancy. Using satellite and reanalysis data, we evaluate this theory by investigating spatiotemporal precipitation variations in six mountainous tropical regions spanning South and Southeast Asia, and the Maritime Continent. We show that a strong relationship holds in these regions between daily precipitation and a measure of convective plume buoyancy. This measure depends on boundary layer thermodynamic properties and lower-free-tropospheric moisture and temperature. Consistent with the theory, temporal variations in lower-free-tropospheric temperature are primarily modulated by orographic mechanical lifting through changes in cross-slope wind speed. However, winds directed along background horizontal moisture gradients also influence lower-tropospheric moisture variations in some regions. The buoyancy measure is also shown to explain many aspects of the spatial patterns of precipitation. Finally, we present a linear model with two horizontal dimensions that combines mountain wave dynamics with a linearized closure exploiting the relationship between precipitation and plume buoyancy. In some regions, this model skillfully captures the spatial structure and intensity of rainfall; it underestimates rainfall in regions where time-mean ascent in large-scale convergence zones shapes lower-tropospheric humidity. Overall, these results provide new understanding of fundamental processes controlling subseasonal and spatial variations in tropical orographic precipitation.

KEYWORDS: Convection; Orographic effects; Stationary waves; Subseasonal variability

1. Introduction

Mountains shape rainfall distributions in many of Earth's tropical land regions, modifying the thermodynamic environment by interacting with large-scale winds or altering surface fluxes. With over 2.5 billion people living in mountainous areas and another 2 billion in lowland areas depending on mountain water resources (Viviroli et al. 2020), orographic precipitation is currently the main water source for over 55% of the world's population, with a majority of that fraction located in the tropics. It is also the main source of energy for hydropower, which is the primary resource for renewable electricity generation globally, and a potential cause of dam failures when occurring in excess (Li et al. 2022).

Orographic rainfall features large spatial gradients, with vastly different hydrological conditions upwind and downwind of ridges. In the tropics, strong precipitation gradients are widely observed along local orography in South and Southeast Asia, the Maritime Continent, and the northern and central Andes (Fig. 1). The spatial structure of orographic precipitation has been studied in various regions across the tropics, with examples including the Ethiopian Highlands (Van den Hende et al. 2021), the Andes (Espinoza et al. 2015), the Western Ghats (e.g., Tawde and Singh 2015), and the Arakan Yoma range of Myanmar (e.g., Shige et al. 2017). The qualitative picture behind this spatial organization is widely known: mountains force low-level ascent on their upwind flanks, which, with sufficient moisture, drives condensation and precipitation (Smith 1979; Roe 2005). The subsiding downstream flow, conversely, is warm and dry. Yet this paradigm, which assumes layer-wise ascent and saturation, is unlikely to be quantitatively accurate in tropical regions where most rainfall stems from convection (Kirshbaum et al. 2018) and where even simple questions, such as what sets the upstream extent of orographic rainfall enhancement, have been debated (Smith and Lin 1983; Grossman and Durran 1984). This study aims to address this issue and related open questions (such as controls on rain shadow extent and the amplitude of rainfall maxima), taking several tropical regions as examples.

In the midlatitudes, column-integrated water vapor transport (IVT) has been proposed as a dominant control on orographic precipitation (Sawyer 1956; Smith 2019). Indeed, in the idealized picture of forced ascent over an orographic barrier, IVT modulates the condensation rate over the upwind slopes. Additionally, stronger IVT typically results in a smaller nondimensional mountain height (through both stronger winds and a smaller effective static stability), causing flow to ascend rather than detour around mountains (Smith 1989; Kirshbaum and Smith 2008). Other controls on midlatitude orographic precipitation include mountain slope and temperature-mediated microphysical effects (Kirshbaum and Smith 2008). The spatial organization of orographic precipitation in convectively stable flows has been understood through the influence of topography on vertical

Corresponding author: Quentin Nicolas, qnicolas@berkeley.edu

DOI: 10.1175/JCLI-D-23-0340.1

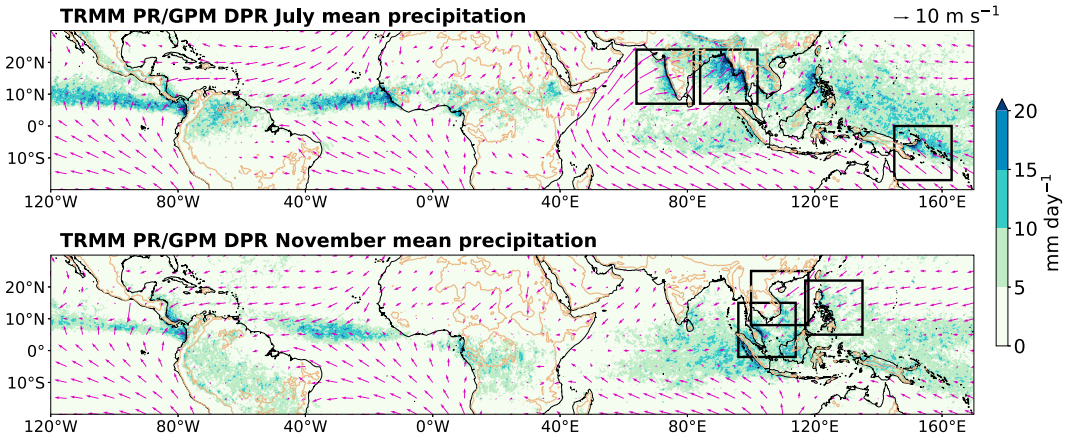

FIG. 1. TRMM PR and GPM DPR near-surface precipitation, 500-m surface height level (thin brown contours), and ERA5 wind vectors 100 m above the surface averaged over (top) July and (bottom) November from 2001 to 2020. See section 2 for details on the data products.

velocities in saturated flows, with a contribution from the downwind advection of hydrometeors (Smith and Barstad 2004, hereafter SB04).

Orographic precipitation generally occurs in association with various types of disturbances, from frontal systems in midlatitude winter to deep convective systems in parts of the tropics (Houze 2012). We illustrate these in Fig. 2, which shows instantaneous radar reflectivity from the Global Precipitation Measurement (GPM) Ku-band radar (Seto et al. 2021) for two cases. The first illustrates a winter frontal system over coastal mountains of British Columbia and features a horizontally wide, vertically shallow signal with a sloping bright band (visible between 300 and 550 km at 2-km altitude in the vertical cross section), characteristic of frontal ascent. In contrast, the Western Ghats case, during the summer monsoon, features smaller-scale, stronger echoes reaching deeper heights (up to 10 km; note that summertime convection in and upstream of the Western Ghats is shallower than in the rest of the tropics;

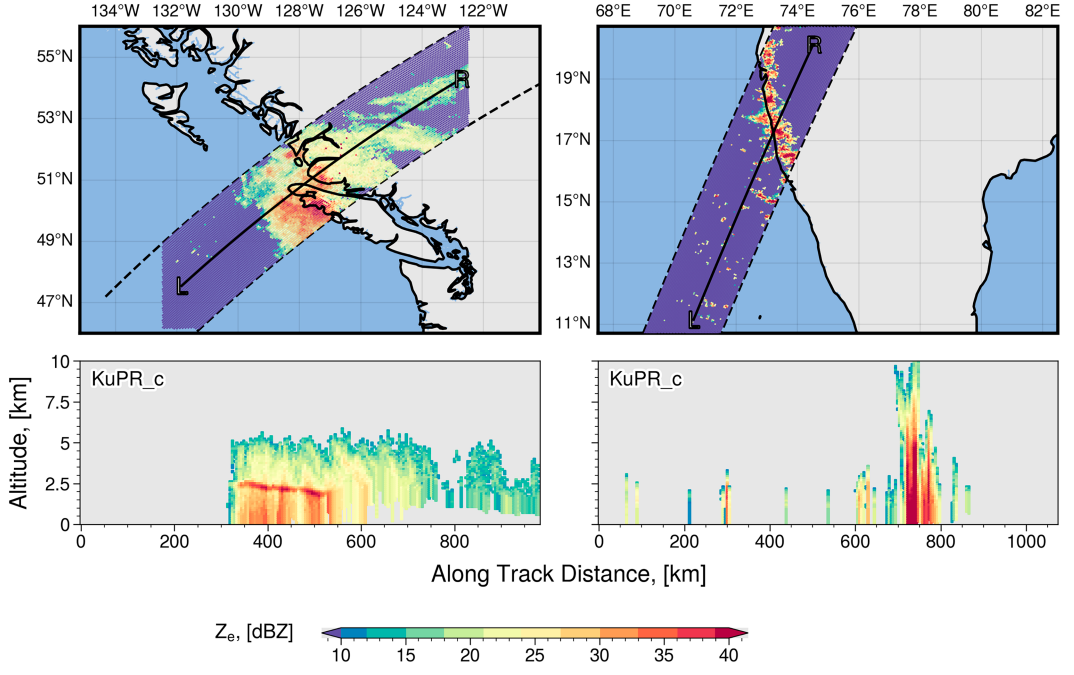

FIG. 2. (top) Near-surface radar reflectivity from the Ku-band GPM radar and (bottom) vertical cross section of corrected Ku-band reflectivity for two overpasses: (left) 11 Feb 2015 (GPM orbit 005434) over the coast range of British Columbia and (right) 19 Jun 2014 (GPM orbit 001735) over the Western Ghats. The black lines in the top panels show the location of the cross sections in the bottom panels, with letters L and R corresponding to the left and right of the cross sections. This figure was produced using the DRpy software package (Chase and Syed 2022).

see Kumar and Bhat 2017). While wide radar echoes are also observed in the tropics, such as in mesoscale convective systems (Houze et al. 2015), such systems reach deeper heights than winter midlatitude storms.

Tropical orographic precipitation has a more even temporal distribution than surrounding continental or oceanic precipitation (Van den Hende et al. 2021; Espinoza et al. 2015; Sobel et al. 2011). Nevertheless, intraseasonal and interannual variability in orographic rainfall seems to be influenced by the classical tropical modes that regulate moist convection. Examples include the boreal summer intraseasonal oscillation (BSISO; Shige et al. 2017; Hunt et al. 2021), the Madden–Julian oscillation (MJO; Bagtasa 2020), and large-scale interannual modes such as El Niño–Southern Oscillation and the Indian Ocean dipole (Yen et al. 2011; Revadekar et al. 2018; Lyon et al. 2006; Smith et al. 2013). Hence, any successful theory for tropical orographic precipitation needs to address the question of how mountains interact with moist convection.

Boundary layer moist static energy and free-tropospheric temperature regulate moist convection by influencing column stability. Observations and simulations have shown that free-tropospheric water vapor also exerts a strong control on precipitation, consistent with the idea that entrainment of free-tropospheric air modulates plume buoyancy (e.g., Derbyshire et al. 2004). Tropical rainfall is thus jointly influenced by free-tropospheric temperature and moisture, and interacts with slower, balanced dynamics to eliminate perturbations in these quantities—a behavior termed lower-tropospheric quasi-equilibrium (QE; e.g., Raymond et al. 2015). The prominent role of lower-tropospheric moisture has been confirmed in observations of orographic convection at low latitudes (Hunt et al. 2021; Nelson et al. 2022). Beyond the lower-tropospheric thermodynamic environment, factors such as the wind profile—especially vertical wind shear, which one could expect to be important in the presence of mountain waves—should affect moist convective development (see, e.g., Robe and Emanuel 2001; Anber et al. 2014; Peters et al. 2022a,b). We do not consider such factors here.

Ahmed et al. (2020) cast the observed dependence of tropical convection on the lower-tropospheric thermodynamic environment into a simple buoyancy-based framework. Precipitation is strongly controlled by a measure of plume buoyancy that takes into account the influences of instability and entrainment, and depends on boundary layer equivalent potential temperature as well as lower-free-tropospheric temperature and moisture. We recently posited (Nicolas and Boos 2022, hereafter NB22) that mechanically forced orographic convection can be understood in this framework, with stationary mountain waves disturbing lower-free-tropospheric thermodynamics, in turn affecting precipitation. We developed a linear model for the spatial distribution of rainfall, combining orographic gravity wave dynamics with the linearized QE closure of Ahmed et al. (2020). That model assumes a simple background state that has horizontally uniform temperature and moisture profiles, with horizontally and vertically uniform wind. At first order, the temperature and moisture perturbations are dictated by vertical displacement in a mountain wave, which is in turn controlled by the topographic shape, cross-slope wind, and static stability. The normalized gross moist stability (e.g., Raymond et al. 2009) appears as a second-order control because it modulates convective moisture relaxation. One goal of the present work is to evaluate to what extent this framework (extended to two horizontal dimensions) can explain observed spatial patterns of orographic tropical rainfall.

More generally, this study explores the physical drivers behind the temporal variations and spatial structure of orographic precipitation around six tropical mountain regions: the Western Ghats (India), the western coast of Myanmar (Arakan Yoma mountain range), the eastern coast of Vietnam (Annam Range), the Malay Peninsula, the Philippines, and the island of New Britain (Papua New Guinea). We justify the use of a lower-tropospheric buoyancy measure in quantifying daily orographic precipitation variability and explore the dominant controls on its components—both within the boundary layer and the lower free troposphere. We then explore to what extent time averages of this buoyancy measure account for observed spatial patterns of rainfall, and test the QE-based linear theory of NB22 against observations.

2. Data

Two precipitation products are used. Seasonal averages (used in sections 1, 3, and 6) are obtained from monthly averages of near-surface precipitation rates from the Tropical Rainfall Measuring Mission Ku-band precipitation radar (TRMM PR 3A25; Tropical Rainfall Measuring Mission 2021) for the January 2001–March 2014 period and the Global Precipitation Measurement dual-frequency precipitation radar (GPM 3DPR; Iguchi and Meneghini 2021) for the April 2014–December 2020 period, both on a 0.25° grid. In section 4, where we require daily resolution, we use the IMERG V06B precipitation dataset (Huffman et al. 2019), which combines satellite-based infrared and passive microwave measurements with rain gauge data to provide hourly estimates at 0.1° resolution. IMERG is known to suffer from biases in regions of complex topography relative to rain gauge measurements, but these biases are reduced when considering spatial averages (Pradhan et al. 2022). We use daily precipitation averages at large spatial scales, and the regions over which we average consist of 45%–80% ocean points, where confidence in IMERG retrievals is higher.

We evaluate the thermodynamic environment and horizontal winds from the ERA5 reanalysis (Hersbach et al. 2018), which provides hourly data at 0.25° resolution. Johnston et al. (2021) showed that moisture soundings from ERA5 had excellent agreement with satellite-based radio occultation retrievals in the tropics and subtropics. Proper evaluation of ERA5 lower-tropospheric temperature is lacking; we note that Hersbach et al. (2020) showed improved 850-hPa temperature estimates (when compared to radiosondes) over ERA-Interim, especially in the past two decades.

Unless otherwise specified, we use topography from the ETOPO1 global relief model (National Geophysical Data Center 2011; Amante and Eakins 2009), at 60-arc-s resolution.

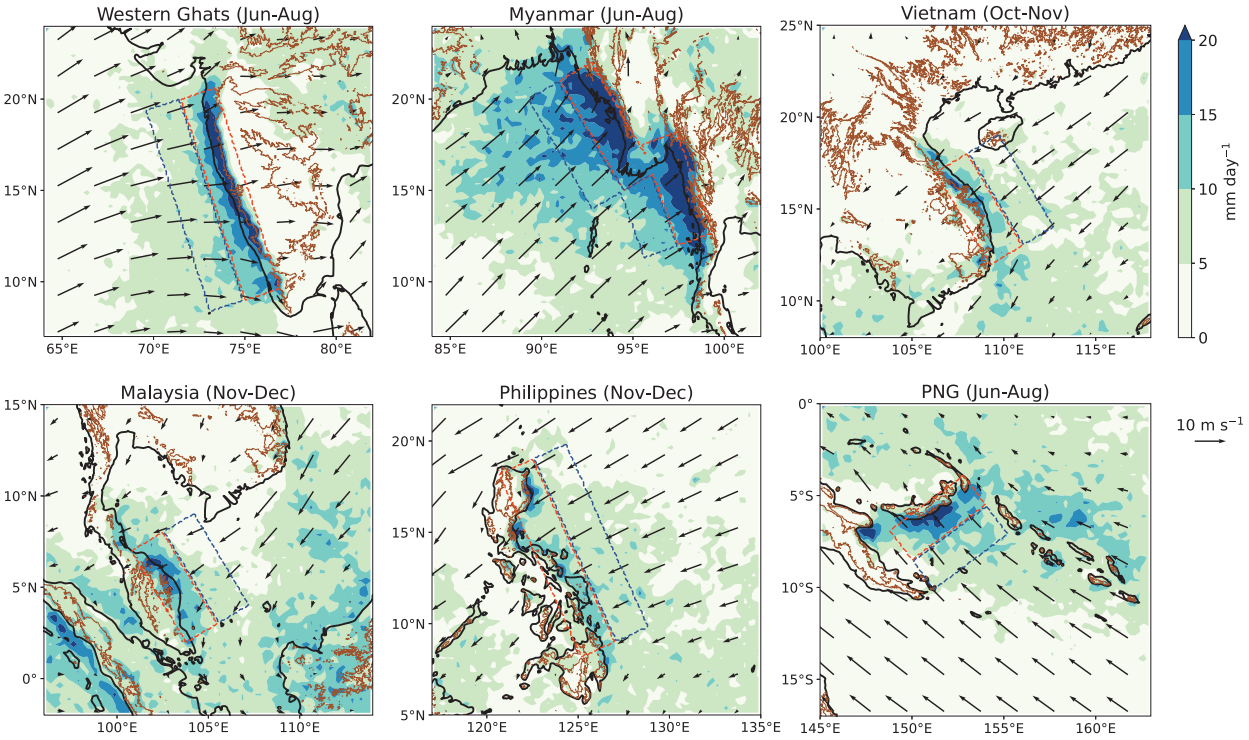

FIG. 3. TRMM PR and GPM DPR near-surface precipitation, 500-m surface height level (thin brown contours), and ERA5 wind vectors 100 m above the surface in six tropical regions, averaged over each region's rainiest season (see text) from 2001 to 2020. The red dashed boxes outline the orographic rainbands, which are analyzed in section 4. The blue dashed boxes define the regions over which cross-slope IVT is averaged in Fig. 5. Here and in later figures, PNG refers to Papua New Guinea.

3. Selecting regions of mechanically forced tropical orographic rainfall

To illustrate the physical drivers of tropical orographic precipitation, we select six regions in South Asia and the Maritime Continent. We focus on mechanically forced convection, a regime in which orographic forcing is felt through the forced uplift of impinging flow, by opposition to thermal forcing, where the diurnal cycle of heating over sloped terrain drives low-level convergence. The wind speed threshold marking the transition from thermal to mechanical forcing depends on various factors including static stability N and mountain height h_m. One quantity often used to characterize orographic flows is the nondimensional mountain height,[1] $M = Nh_m/U$, where U is the cross-slope wind speed. Flows with $M < 1$ tend to cross topography (rather than being blocked upstream), which may prevent the development of thermally forced circulations (Kirshbaum et al. 2018). For moderately high mountains (500–1000 m) in the tropics, various studies have suggested that mechanical forcing dominates above about 5 m s^{-1} (Nugent et al. 2014; Wang and Sobel 2017). Accordingly, we selected six regions with a mean upstream wind (during the local rainy season) higher than 5 m s^{-1} and a visible orographic rainband. This sample is not an exhaustive representation of tropical orographic rainfall, although we think it is quite representative of mechanically forced cases. These regions are outlined in Fig. 1, with close-up views of their topography and seasonal-mean rainfall and wind in Fig. 3. The rainfall maps have some visible noise because they are only based on TRMM and GPM radar overpasses, which have sparse temporal coverage.

For each region, we analyze data over a 20-yr period (2001–20) during the local rainiest season (which also corresponds to a mechanically forced regime), defined below for each specific case. Two regions (Vietnam and the Philippines) experience a second rainfall peak in boreal summer on the other side of their mountain ranges, associated with reversed winds during the summer monsoon (see Fig. 1). Because the winds are not as strong then, the dominance of mechanical forcing cannot be clearly established, and we did not include these secondary rainy seasons in our analysis. In section 4, we analyze daily data averaged over the orographic rainbands; these rainbands are defined manually using rectangular boxes and are outlined in red in Fig. 3. We summarize key information about each region in Table 1, and describe these in detail hereafter.

Three of these regions have their rainiest season in boreal summer (June–August). The Western Ghats, a mountain range on the west coast of peninsular India, form a kilometer-high barrier to the southwesterly monsoon flow. With $M \simeq 0.8$ (measuring wind speed 500 km upstream of the coast and 100 m above the surface to avoid influences from surface friction and flow deceleration by topography), the Ghats fall within

[1] The M is also the inverse of a Froude number.

TABLE 1. Key information about the regions studied. Here and in later tables, PNG refers to Papua New Guinea.

Region name	Rainy season considered in this study	Nondimensional mountain height
Western Ghats	June–August	0.8
Myanmar	June–August	0.8
Vietnam	October–November	1
Malaysia	November–December	0.5
Philippines	November–December	0.3
PNG	June–August	0.4

a clear mechanically forced regime, as attested by the small diurnal cycle of rainfall there (Shige et al. 2017). The dynamics of orographic precipitation in the Western Ghats have been the subject of several modeling studies (Smith and Lin 1983; Grossman and Durran 1984; Ogura and Yoshizaki 1988; Xie et al. 2006; Oouchi et al. 2009; Sijikumar et al. 2013; Zhang and Smith 2018). These studies confirm that the presence of orography is crucial in producing the observed rainband, and (expectedly) that latent heating cannot be neglected in describing the orographic flow. Past literature has also discussed the location of the rainfall maximum upstream of the Western Ghats. While some studies initially suggested that it occurred upstream of the coastline (e.g., Xie et al. 2006), Shige et al. (2017) determined that it was positioned over the western slopes of the Ghats (consistent with Fig. 3).

The Arakan Yoma mountain range, located along the coast of Myanmar, also interacts with the Asian summer monsoon (Oouchi et al. 2009; Wu et al. 2018). With maximum seasonal-mean precipitation values exceeding 30 mm day^{-1} upstream of the range, it is responsible for the strongest rainband (in terms of mean precipitation rate) on Earth in boreal summer. This precipitation maximum is located along the coast (see Fig. 3 and Shige et al. 2017). Compared to the Western Ghats, convection is deeper and of wider scale upstream of Myanmar, a fact that Shrestha et al. (2015) associated with differences in lower tropospheric humidity; M has a similar value around 0.8 there.

The island of New Britain, in Papua New Guinea (PNG), is our third region of interest in boreal summer. The mountains are of modest height there (300 m when averaging across the island, although individual peaks exceed 2 km), but a strong precipitation band reaching 25 mm day^{-1} lies upstream of the island. Winds speeds around 8–9 m s^{-1} yield a nondimensional mountain height $M \simeq 0.4$. Orographic rainfall in PNG has been the focus of a few studies (e.g., Biasutti et al. 2012; Smith et al. 2013).

The remaining three regions are associated with boreal autumn rainfall. The coast of Vietnam, east of the Annam range, receives most of its rainfall in October and November (Chen et al. 2012; Ramesh et al. 2021), with an onshore cross-slope wind of 8–9 m s^{-1} during this season ($M = 1$). The eastern coast of the Philippines experiences a late autumn precipitation peak (November–December) with a similar wind speed and $M = 0.3$ (Chang et al. 2005; Robertson et al. 2011). Finally, the eastern half of the Malay Peninsula also receives most of its rainfall in November and December (Chen et al. 2013), similarly associated with mechanical orographic forcing ($M = 0.5$).

TABLE 2. Percentage of seasonal rainfall contributed by the rainiest days (defined as days and locations where rainfall is above the 90th percentile), in the whole region and within the orographic rainband, for each region studied. The rainbands are defined by the red dashed rectangles in Fig. 3.

Region name	Whole region	Orographic rainband
Western Ghats	74	53
Myanmar	59	43
Vietnam	80	73
Malaysia	63	61
Philippines	76	66
PNG	70	55

4. Controls on daily variations of orographic rainfall

In the tropics, mechanically forced orographic rainfall is subject to less temporal variability than rainfall over surrounding land and ocean. In particular, it has a weak diurnal cycle, as noted by Shige et al. (2017) in the Western Ghats and in Myanmar (see also Aoki and Shige 2024). This can be understood as resulting from daytime heating of the boundary layer being limited by the ventilation resulting from strong wind (e.g., Nugent et al. 2014). The distribution of daily rainfall within regions where mechanical forcing dominates is also more uniform, with less contribution from extreme days. This was noted by Espinoza et al. (2015) in the central Andes and is confirmed for regions studied here (Table 2). Nevertheless, these regions still show substantial subseasonal rainfall variations. The goal of this section is to determine the factors governing these temporal variations of daily mean precipitation.

a. *Dynamic and thermodynamic predictors of daily rainfall variations*

The canonical picture of orographic rainfall highlights the importance of the cross-slope vapor transport in governing rain rates (Smith 2019). In a saturated atmosphere ascending with velocity w, the column-integrated condensation rate is

$$C = -\int_0^\infty w \frac{d(\rho q_{\mathrm{sat}})}{dz} dz. \tag{1}$$

The water vapor density can be approximated as decreasing exponentially with z, with a scale height H_{sat}. If $\mathbf{u}$ denotes the surface horizontal wind and h the surface height, then $w(z = 0) = \mathbf{u} \cdot \nabla h$. In the simplest approximation where w is vertically uniform, then

$$C = \int_0^\infty (\mathbf{u} \cdot \nabla h) \frac{\rho q_{\mathrm{sat}}}{H_{\mathrm{sat}}} dz \simeq \frac{\mathbf{IVT} \cdot \nabla h}{H_{\mathrm{sat}}}, \tag{2}$$

where **IVT** denotes the vertically integrated water vapor transport. Setting precipitation equal to the product of C with

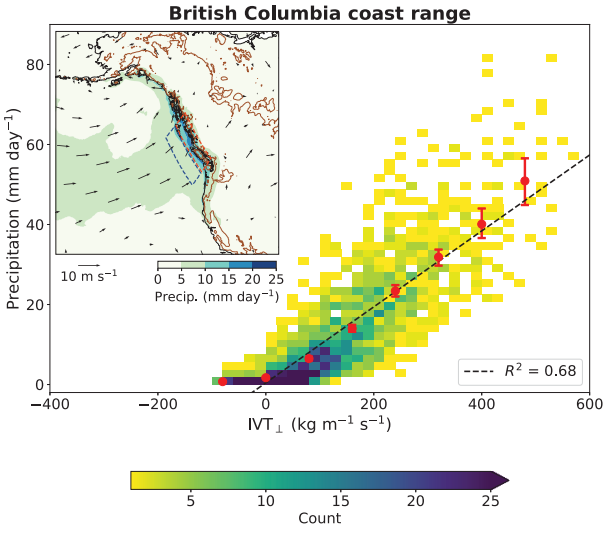

FIG. 4. Joint distributions of daily cross-slope IVT and precipitation in the coast range of British Columbia. Precipitation is averaged over the orographic rainband (red box in the inset). Cross-slope IVT (defined as its northeastward component) is averaged immediately upstream of the precipitation maximum (blue dashed box in the inset). The black dashed line shows the best linear fit. The red dots represent conditionally averaged precipitation over bins of width 80 kg m^{-1} s^{-1}, with error bars representing a 95% confidence interval obtained by bootstrapping. The inset shows climatological rain (IMERG) and 100 m wind (ERA5) averaged over November–January.

a precipitation efficiency, one sees that in this so-called upslope model, it is proportional to the cross-slope IVT. This model has several shortcomings, including the assumption of a saturated atmosphere and the oversimplified vertical velocity parameterization. Nevertheless, it skillfully characterizes temporal rainfall variations in some midlatitude mountain ranges, as illustrated for the British Columbia coastal range in Fig. 4; despite some scatter, daily precipitation rates in winter are decently described by a linear relationship with cross-slope IVT (hereafter IVT$_\perp$). Although the vertically uniform ascent model for vertical velocity ($w = \mathbf{u} \cdot \nabla h$) is crude, it captures the simple fact that vertical velocities in convectively stable orographic flows are controlled by cross-slope wind. Deviations from this simple picture, including effects of stratification, wind shear, and the specific dynamics of various types of weather systems, yield the scatter.

In the tropics, where convective ascent is more important, one might expect other factors than cross-barrier winds to modulate ascent rates. Still, Bagtasa (2020) suggested that enhanced cross-slope winds in the Philippines associated with certain phases of the MJO favored rainfall in late autumn. Similarly, Shige et al. (2017) showed that rainfall in the Western Ghats and the Arakan Yoma range of Myanmar was in phase with the southwesterly wind strength modulated by the BSISO. This suggests that cross-slope winds, and perhaps cross-slope IVT, still are important controls on orographic precipitation at low latitudes. Figure 5 (first and third columns) shows the joint distributions of IVT$_\perp$ and precipitation, as well as precipitation conditionally averaged on IVT$_\perp$.[2] While a positive relationship remains, it does not hold as strongly as in the midlatitude winter case shown in Fig. 4, with numerous dry days associated with strong IVT$_\perp$. Therefore, we attempt to find another variable to characterize temporal variations in tropical orographic rainfall, starting with thermodynamic metrics that have been associated with convective rainfall.

The question of what environmental factors set convective precipitation rates is at the heart of any theory of tropical atmospheric dynamics. The QE hypothesis (e.g., Emanuel et al. 1994) states that convection acts to deplete anomalies in convective available potential energy (CAPE). This description predicts the effect moist convection has on its environment, consuming instability and setting vertical temperature profiles close to moist adiabats. However, it alone does not provide information on convective intensity or precipitation rates, given environmental conditions. One further development stems from the observed exponential dependence of precipitation rates on column moisture content (e.g., Bretherton et al. 2004). The physical roots of this dependence lie in the effect that entrainment of free-tropospheric air has on plume buoyancy.

Seeking a unified measure that would characterize rainfall across the tropics, Ahmed and Neelin (2018) derived an expression for a lower-tropospheric averaged plume buoyancy that only depends on environmental temperature and moisture profiles. Dividing the lower atmosphere in two layers, a boundary layer (subscript B) and a lower-free-troposphere[3] (subscript L), this expression reads (Ahmed et al. 2020)

$$B_L = g\left(\alpha_B \frac{\theta_{eB} - \theta^*_{eL}}{\theta^*_{eL}} - \alpha_L \frac{\theta^*_{eL} - \theta_{eL}}{\theta^*_{eL}}\right), \tag{3}$$

where g is the acceleration of gravity, θ_e is equivalent potential temperature (and θ^*_e its saturated value), and subscripts denote averages taken over respective layers. The weights α_B and $\alpha_L = 1 - \alpha_B$ depend on the thickness of each layer and the assumed mass flux profile of the plume. We use $\alpha_B = 0.52$ (as in Ahmed et al. 2020). The first term in (3) is a CAPE-like term, wherein the difference between boundary layer θ_e and

[2] Throughout this manuscript, conditionally averaging A on B means averaging A over days where B is in a given range of values. Where relevant, the ranges of values are defined in the figure captions.

[3] Here, the boundary layer is defined as between the surface and 900 hPa, and the lower free troposphere between 900 and 600 hPa. We chose these definitions (over using a fixed-depth boundary layer and variable-depth lower free troposphere) so that lower-free-tropospheric averages are not affected by surface elevation changes. Points where the surface pressure is lower than 900 hPa are masked out of all analyses. These represent a small fraction of each domain and can be visualized as the white shaded regions in Fig. 11. The analyses are robust to the exact definition of the boundary layer top; changing it to 875 or 925 hPa does not significantly affect any of the results presented. Moreover, daily variations in boundary layer height (as determined by ERA5) are modest in the rain bands analyzed in Figs. 5–10, with standard deviations lower than 15 hPa.

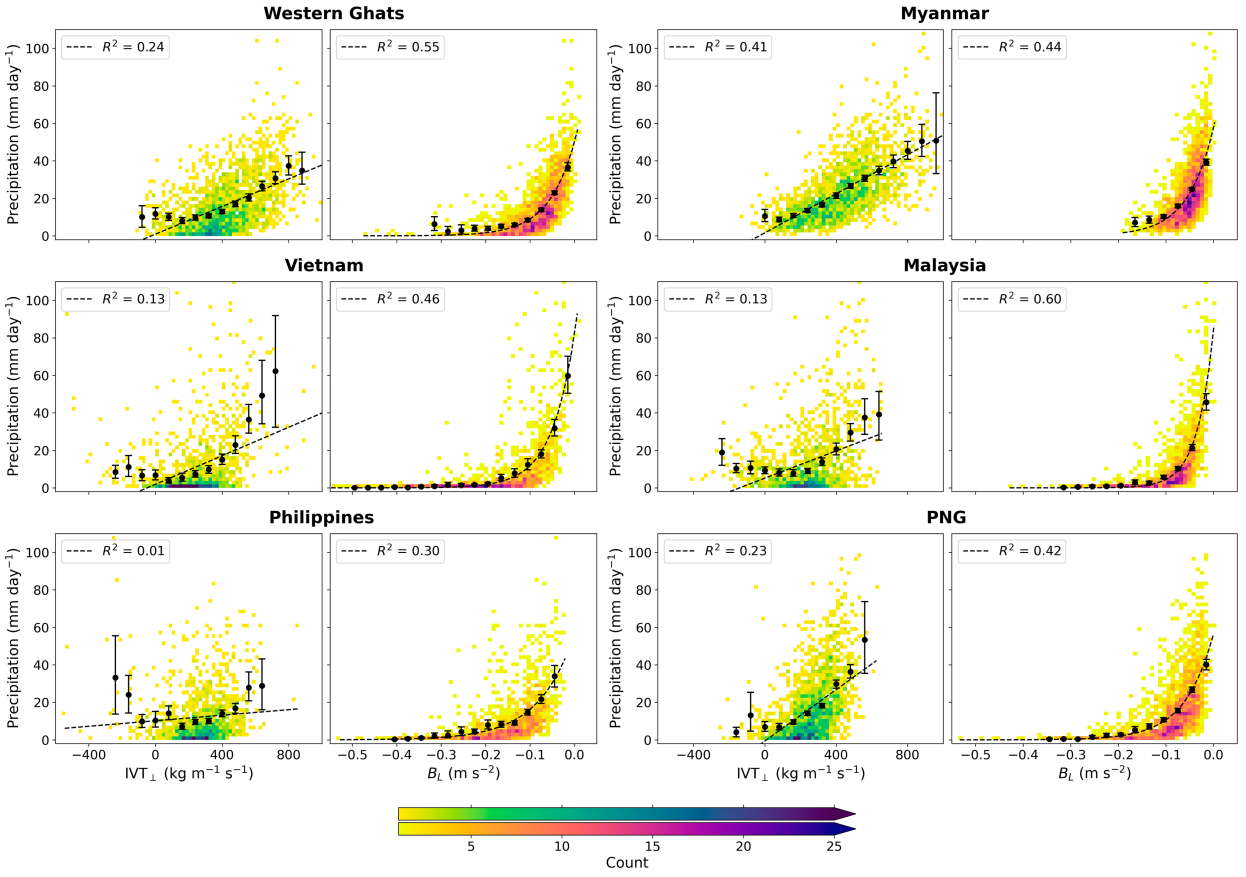

FIG. 5. Joint distributions of daily cross-slope IVT and precipitation (first and third columns; green colors) and B_L and precipitation (second and fourth columns; red colors). Here, B_L and precipitation are averaged spatially over the rainband regions (red boxes in Fig. 3). IVT is averaged right upstream of the rainband regions (blue boxes in Fig. 3). The cross-slope direction is defined as 70° (Ghats), 60° (Myanmar), 240° (Vietnam), 225° (Malaysia), 225° (Philippines), and 320° (PNG). Linear fits (for the IVT–precipitation relation) and exponential fits (for the B_L–precipitation relation) are shown as dashed lines, with the associated coefficients of determination in the legend. The black dots represent conditionally averaged precipitation over bins of width 80 kg m^{-1} s^{-1} (for IVT) and 0.03 m s^{-2} (for B_L), with error bars representing a 95% confidence interval obtained by bootstrapping.

lower-free-tropospheric θ_e^* provides a measure of moist convective instability. The second term describes subsaturation of the lower free troposphere, and quantifies the efficiency of entrainment at reducing buoyancy by drying the plume (hence the negative sign in front of it).

When conditionally averaged on B_L [at $\mathcal{O}(10)$ km and hourly scale], precipitation is near-zero for negative values and strongly increases above zero buoyancy, a behavior reminiscent of its exponential dependence on column moisture. The strength of this precipitation-buoyancy relationship lies in its universality, as it holds over all tropical oceans, and, with slight modifications, over tropical land (Ahmed et al. 2020). Using conditional averages reduces the scatter in precipitation rates associated with a given value of B_L. This spread can be due to both stochasticity or ignored physical effects (e.g., higher-order dependencies on the vertical structure of environmental temperature and moisture, or wind shear effects). Figure 5 (second and fourth columns) shows the joint distribution of precipitation and B_L for each region, using daily-mean data spatially averaged over the rainbands (red boxes in Fig. 3). Spatially averaging the nonlinear rainfall–B_L relationship is expected to smooth out the sharp increase around zero buoyancy; hence, we show exponential fits [rather than ramp fits of the form max(0, $aB_L + b$)] with the joint distributions. We also show conditional averages at various B_L values. Plume buoyancy B_L is more skillful than IVT$_\perp$ at capturing daily rainfall variations in all regions except perhaps Myanmar, where the range of B_L is narrower than in other regions (during the summer monsoon, the coast of Myanmar is in a precipitating state most of the time). It is notable that B_L characterizes rainfall with similar accuracy in regions that have different convective vertical structures (Kumar and Bhat 2017; Shige and Kummerow 2016). This indicates that B_L is not only suitable to quantify rainfall from deep convection, but that it is also an adequate measure in regions where precipitation tops frequently lie around 4–6 km. We next decompose variations in B_L into contributions from its components to understand the origins of precipitation variability in tropical orographic regions.

Note that B_L is a function of three variables: θ_{eB}, θ_{eL}, and θ_{eL}^* [Eq. (3)]. Alternatively, following Ahmed et al. (2020),

it can be viewed as a function of θ_{eB}, T_L, and q_L, where T is temperature and q denotes specific humidity, hereafter in temperature units (i.e., multiplied by the ratio of the latent heat of vaporization of water L_v to the heat capacity of air at constant pressure c_p). In this description, plume buoyancy is affected by boundary layer θ_e (which affects lower-tropospheric stability), lower-free-tropospheric temperature (affecting both stability and lower-free-tropospheric subsaturation) and lower-free-tropospheric moisture (affecting only the subsaturation component). To evaluate the sensitivity of B_L to each component, we linearize its expression:

$$\delta B_L = \frac{\partial B_L}{\partial \theta_{eB}} \delta\theta_{eB} + \frac{\partial B_L}{\partial T_L} \delta T_L + \frac{\partial B_L}{\partial q_L} \delta q_L, \tag{4}$$

where δ denotes a deviation from a time average, $\partial B_L/\partial\theta_{eB} = g\alpha_B/\theta^*_{eL}$, and the expressions for $\partial B_L/\partial T_L$ and $\partial B_L/\partial q_L$ are given in Ahmed et al. (2020) (these expressions were derived from a simplified version of B_L that is very close to the one employed here). Here, we use fixed values of $\partial B_L/\partial\theta_{eB} = 0.014\ \mathrm{m\ s^{-2}\ K^{-1}}$, $\partial B_L/\partial T_L = -0.058\ \mathrm{m\ s^{-2}\ K^{-1}}$, and $\partial B_L/\partial q_L = 0.014\ \mathrm{m\ s^{-2}\ K^{-1}}$, which have little dependence on the specific base state considered.

Figure 6 examines the contribution of each term on the right-hand side of (4) to variations in B_L, over the Western Ghats and PNG. For example, to estimate the contribution of θ_{eB} variations to B_L variations, we fix T_L and q_L and estimate the B_L perturbations that would have occurred if only θ_{eB} had varied, i.e., $(\partial B_L/\partial\theta_{eB})\delta\theta_{eB}$. We regress δB_L on this measure and show the joint distribution of both quantities (top panels), then repeat the same analysis with $(\partial B_L/\partial T_L)\delta T_L$ (middle panels) and $(\partial B_L/\partial q_L)\delta q_L$ (bottom panels). It is apparent from these univariate linear regressions that q_L dominates B_L variations in both regions. This is true even though B_L is 4 times more sensitive to T_L ($|\partial B_L/\partial T_L| \simeq 4\partial B_L/\partial q_L$). Indeed, variations of q_L are less constrained than those of T_L: lower-free-tropospheric temperature anomalies are quickly smoothed in the tropics by gravity waves, resulting in a state of weak temperature gradients (e.g., Sobel et al. 2001). Over the Western Ghats, T_L variations still account for 28% of the variance in B_L, while θ_{eB} variations do not correlate with B_L. In PNG, the converse picture holds. Figure 7 shows the coefficients of determination (R^2) of the regression lines that appear in Fig. 6, extended to all regions. In addition, we perform bivariate linear regressions of δB_L against θ_{eB} and T_L, θ_{eB} and q_L, and T_L and q_L (we omit $\partial B_L/\partial\theta_{eB}$ and other prefactors as these only change the regression coefficients, and not the R^2). From the univariate regressions alone, there seem to be two types of behavior: one where buoyancy variations are controlled by lower-free-tropospheric thermodynamic quantities (the Western Ghats and Myanmar), and the other where boundary layer θ_e and lower-free-tropospheric moisture set these variations (Vietnam, Malaysia, the Philippines, and PNG). However, the bivariate regressions show that in all regions, T_L and q_L account together for the highest fraction (over 85%) of the variance in B_L. Consistently, the rest of this section focuses primarily on the factors governing T_L and q_L variations.

An important caveat is that the three variables that control variations in lower tropospheric buoyancy B_L are not independent of each other. In QE theory, convection rapidly reduces CAPE variations, tying free-tropospheric saturation equivalent potential temperature θ^*_e to subcloud layer equivalent potential temperature θ_{eB}. Thus, one expects θ_{eB} and T_L to exhibit substantial correlation. Indeed, correlation coefficients between daily θ_{eB} and T_L averaged over the orographic precipitation bands vary between 0.7 and 0.9 in all regions. However, this relationship only indicates that θ_{eB} and θ^*_{eL} covary, and does not provide insight into B_L variations because B_L depends on $\theta_{eB} - \theta^*_{eL}$, as in (3). Additionally, turbulent exchange between the subcloud layer and the lower free troposphere produces smaller correlations (0.3–0.6) between daily θ_{eB} and q_L variations. T_L and q_L are essentially uncorrelated across all regions.

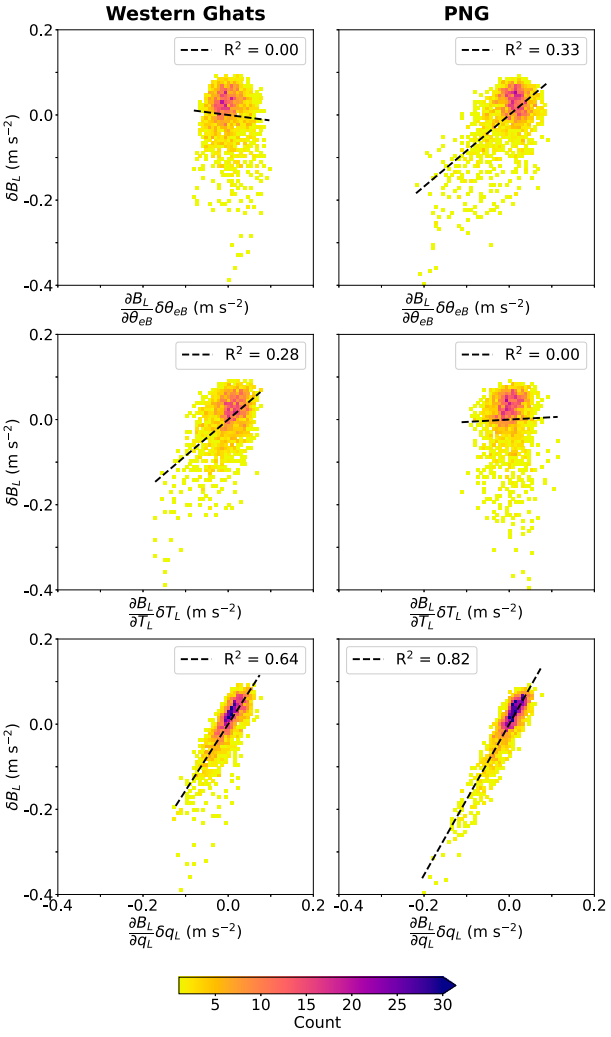

FIG. 6. Joint distributions of buoyancy anomalies δB_L and their contribution from (top) θ_{eB} anomalies, (middle) T_L anomalies, and (bottom) q_L anomalies for two regions illustrating different regimes: (left) the Western Ghats and (right) PNG. For each plot, δB_L is also regressed on the individual contribution $(\partial B_L/\partial V)\delta V$ where $V = \theta_{eB}$, T_L, or q_L. Black dashed lines show the best fit linear regression.

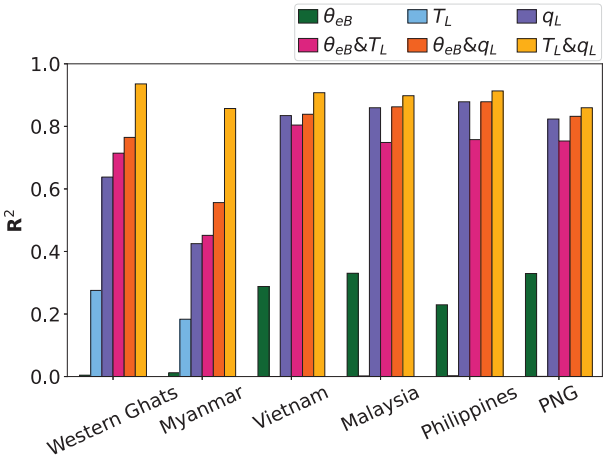

FIG. 7. Coefficients of determination (R^2) from linear regressions of δB_L against its individual contributions from θ_{eB}, T_L, and q_L anomalies (see Fig. 6), as well as joint contributions from pairs of these variables. Note that despite differences in the univariate R^2 across regions (with θ_{eB} anomalies accounting for more variance in B_L than T_L anomalies in a univariate sense), the (T_L, q_L) pair explains the highest fraction of variance in δB_L in all regions.

To link this analysis back to precipitation variations, we compute correlations between daily values of rainfall and each of θ_{eB}, T_L, and q_L upstream of each of the mountain ranges studied (Table 3). These correlations are only a crude measure of the association of each component with precipitation, given that the precipitation–buoyancy relationship is expected to be nonlinear. Nevertheless, a few of the observations made above hold: q_L has the strongest association with precipitation, T_L anomalies are negatively associated with precipitation (recall that $\partial B_L/\partial T_L < 0$), and θ_{eB} has a weak positive association with rainfall.

b. Controls on daily θ_{eB} variations

In this work, the boundary layer extends between the 900-hPa level and the surface—which loosely corresponds to the subcloud layer. Boundary layer θ_e, or equivalently subcloud entropy, is set by exchanges with the surface and the lower free troposphere, with a small contribution from radiative cooling (Emanuel et al. 1994). Entropy exchanges at the top of the boundary layer are twofold: one contribution being in the form of quasi-continuous turbulent mixing across the top of the layer, the other one arising from penetrative convective downdrafts. Over ocean, sea surface temperature (SST) is often the dominant quantity affecting subcloud entropy (e.g., Lindzen and Nigam 1987). Because the orographic rainbands of interest in this section are in close proximity to the sea, one might expect SSTs to exert a strong control on θ_{eB}. We verify this fact in Table 3: SST strongly correlates with θ_{eB} at the daily scale, with correlation coefficients between 0.5 and 0.8 in all regions.

Other factors such as surface wind speed variations or convective downdrafts contribute to variations in θ_{eB} on shorter time scales than SST changes. Because there is no clear influence of orographic mechanical forcing on any of these factors, we do not delve deeper into this topic.

TABLE 3. Correlations between daily precipitation (P) and the three quantities affecting plume buoyancy (θ_{eB}, T_L, and q_L), and between daily SST and boundary layer equivalent potential temperature θ_{eB}. Precipitation, θ_{eB}, T_L, and q_L are averaged over the red boxes in Fig. 3, and SST is averaged over the ocean part of each box.

Region name	$P-\theta_{eB}$	$P-T_L$	$P-q_L$	SST $-\theta_{eB}$
Western Ghats	0.19	−0.15	0.56	0.80
Myanmar	0.16	−0.18	0.30	0.53
Vietnam	0.23	0.03	0.53	0.61
Malaysia	0.17	−0.18	0.51	0.69
Philippines	0.12	−0.06	0.50	0.56
PNG	0.15	−0.15	0.51	0.60

c. Controls on daily lower-free-tropospheric temperature variations

Topographically forced gravity waves carry temperature perturbations. In the canonical picture of mechanical orographic forcing, a mountain of height h_m is placed in a stratified atmosphere (with buoyancy frequency N) with a uniform background horizontal wind U. When the nondimensional mountain height $Nh_m/U \lesssim 1$, the flow ascends over the mountain, creating (by adiabatic cooling) a cold anomaly in the lower-free-troposphere upstream. The stronger the wind, the deeper the ascent region, hence the colder the anomaly. In the case of an idealized ridge of height 1 km, the sensitivity of the temperature perturbation to the impinging wind is (see the appendix)

$$\frac{\partial T_L'}{\partial U} \simeq -0.2\,\mathrm{K}\,(\mathrm{m\,s^{-1}})^{-1}. \tag{5}$$

We now seek to verify whether T_L variations in our regions have patterns that are consistent with this picture. Figure 8 shows time-mean T_L maps in all six regions. Cold anomalies (of around 0.5 K) are visible in each region's rainband, indicated by poleward (in the Western Ghats and Myanmar) or equatorward (in Vietnam, the Philippines, and PNG) excursions of isotherms upstream of and above the topography. These anomalies are consistent with the idea of upstream cooling by orographic lifting in the mean state. To study temporal variations in the strength of this cool anomaly, we average T_L upstream of each mountain range to obtain daily time series. Because the mountains are of modest height in each region, we expect mountain waves to be dominantly affected by winds in the lowermost kilometer of the troposphere. We thus average horizontal winds within the boundary layer and regress them on the T_L time series at each location. The resulting wind vectors are multiplied by −1 so that onshore cross-slope flow corresponds to negative temperature perturbations, and shown in Fig. 8. If our simple estimate (5) were to hold, regressed winds would have a magnitude around 5 m s^{-1} K^{-1} for a 1-km-high mountain.

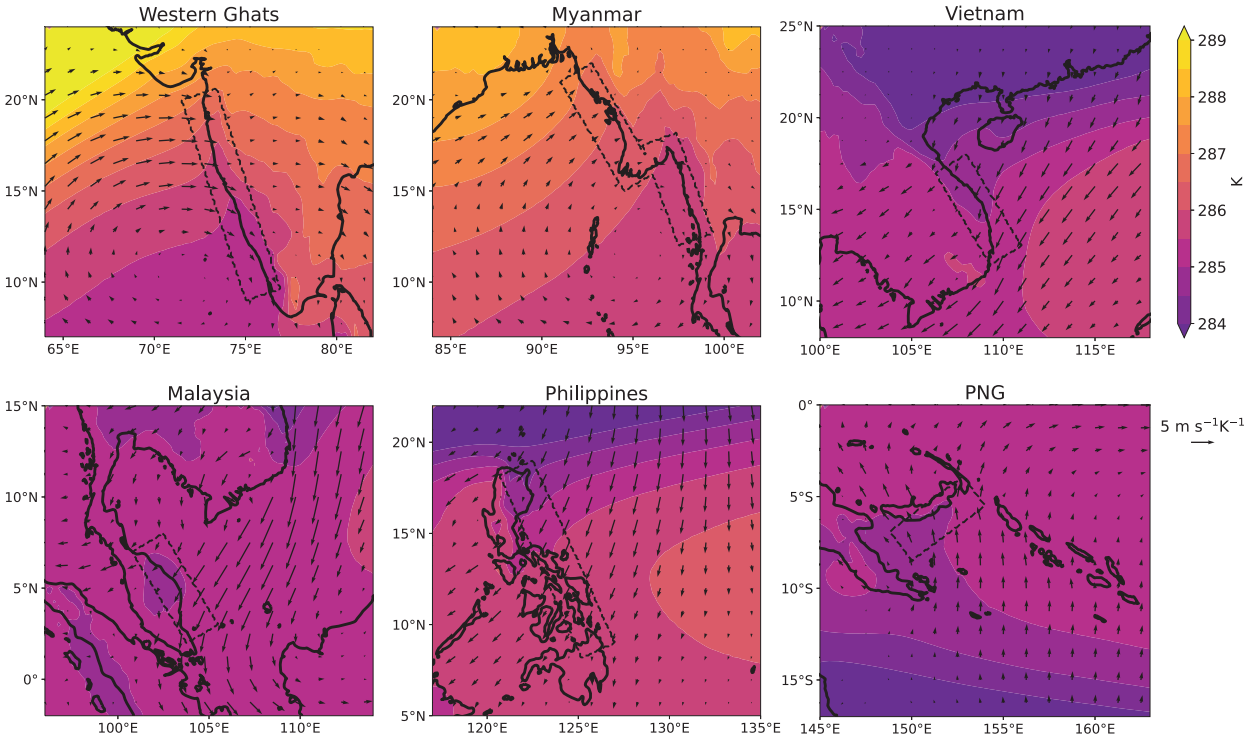

FIG. 8. Boundary layer horizontal wind regressed on lower-free-tropospheric temperature (T_L; averaged in the dashed boxes). The result is multiplied by -1 so that upslope flow is associated with negative temperature perturbations. The color shading shows seasonal-mean T_L. Arrows are masked where neither the u wind regression nor the v wind regression satisfy the false discovery rate criterion (Wilks 2016) with $\alpha = 0.01$.

The wind regressions are directed onshore and cross-slope in each region, which is again consistent with the idea that T_L is modulated by the strength of stationary mountain waves. Furthermore, the magnitude of the regression vectors upstream of each region (except Myanmar) is around 2–5 m s^{-1} K^{-1}, consistent with (5). It is apparent from Fig. 8 (especially in the Philippines, Vietnam, and PNG) that cold anomalies are also associated with up-temperature-gradient winds: background temperature gradients are not everywhere small in these tropical regions, and accordingly cooling can happen through horizontal advection.

d. *Controls on daily lower-free-tropospheric moisture variations*

Given the dominant control q_L exerts on lower tropospheric buoyancy (Fig. 6), understanding drivers of its temporal changes is key to understanding rainfall variations. In the same way they bear temperature anomalies, mountain waves carry moisture perturbations through vertical displacements in a background profile of specific humidity. Rising air upstream of a mountain moistens the lower free troposphere, while downstream subsidence dries it. The magnitude of this effect is estimated using linear mountain wave theory in the appendix. In this idealized picture, the sensitivity of the upstream moisture perturbation to the cross-slope wind is

$$\frac{\partial q_L'}{\partial U} \simeq 0.5\,\mathrm{K}\,(\mathrm{m\,s^{-1}})^{-1}. \tag{6}$$

Once again, this effect neglects any convective response: mountain-induced T_L and q_L perturbations result in enhanced convection, which, in turn, dries the troposphere. A framework to understand the response of convection to thermodynamic perturbations in a mountain wave is presented in section 6. Solving for q_L' in this framework reduces the sensitivity in (6) by about half.

In the absence of horizontal gradients in the background moisture profile, q_L perturbations would be dominantly due to the time-mean ascent perturbation imposed by the terrain, which is well described by stationary mountain waves for a mechanically forced regime (NB22). In Earth's tropics, however, water vapor is far from horizontally homogeneous. This is apparent in Fig. 9, where color shading represents the time-mean q_L in each region: horizontal moisture gradients are much stronger than T_L gradients. Although the impact of orography on the mean q_L distribution is less apparent compared to T_L (because of the stronger background q_L variations), it seems to be associated with moisture contours deviating southward in Myanmar and northward in the Philippines (corresponding to positive anomalies); a local maximum is also present over PNG. Given the background horizontal moisture gradients and the moisture perturbations around orography in Fig. 9, one might expect variations in q_L to be influenced by both winds along the background moisture gradient and winds across orographic slopes.

The vectors in Fig. 9 show horizontal winds regressed on upstream-averaged q_L. In the Western Ghats and Myanmar,

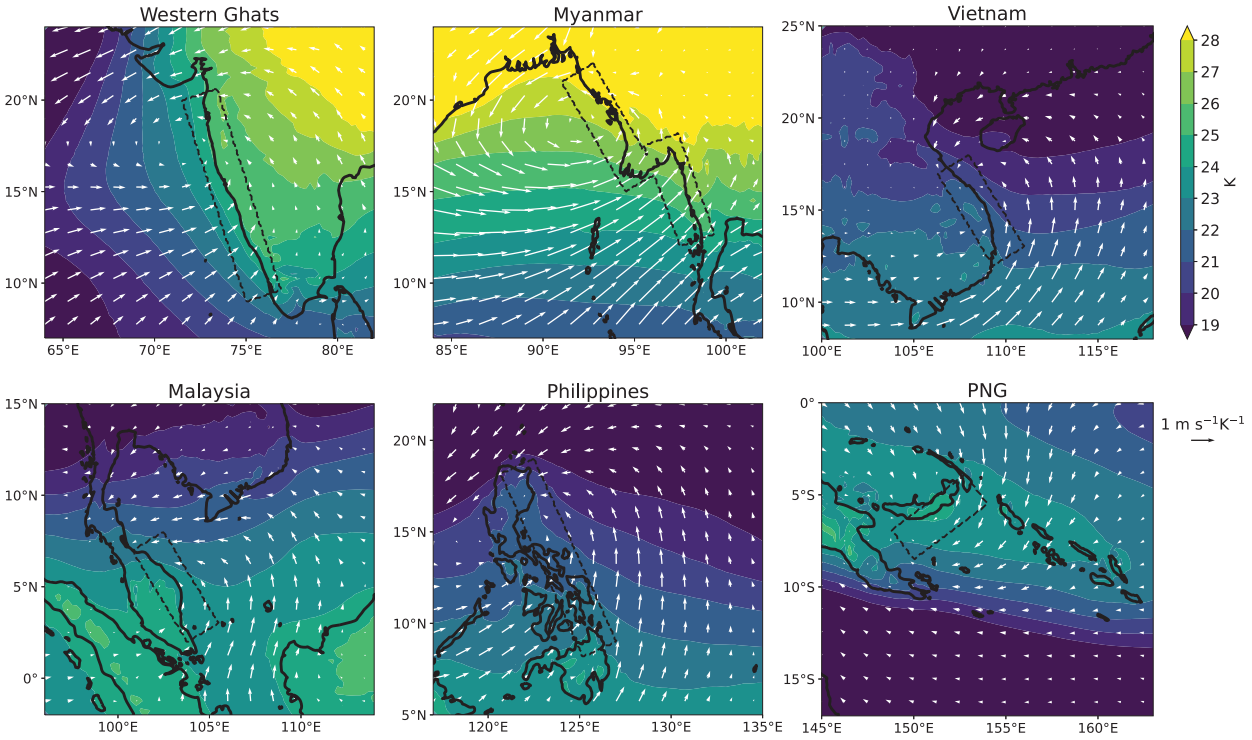

FIG. 9. Boundary layer horizontal wind regressed on lower-free-tropospheric moisture (q_L, averaged in the dashed boxes, in temperature units). The color shading shows seasonal-mean q_L. Arrows are masked using the same criterion as in Fig. 8.

moist perturbations are mostly associated with cross-slope winds, following the theoretical picture of mechanical forcing. The magnitude of the regressions (1–2 m s^{-1} K^{-1}) is somewhat smaller than expected from (6); one would expect 2–4 m s^{-1} K^{-1} when accounting for the correction due to convective feedback (see above). The fact that both negative T_L and positive q_L perturbations—hence positive B_L perturbations—are favored by cross-slope winds in the Ghats and Myanmar explains why IVT$_\perp$ characterizes precipitation better there than in other regions (Fig. 5).

In Vietnam, Malaysia, and the Philippines, regressed winds have little cross-slope flow component: they are mostly directed down mean moisture gradients. In these regions, moistening of the lower free troposphere thus seems to be more effectively attained through large-scale horizontal moisture advection than mechanical forcing of upslope flow. This result contrasts with the intuitive view that mechanically forced orographic precipitation and accompanying lower-tropospheric humidity variations are mostly controlled by forced ascent, i.e., by the strength of upslope flow. It shows that, despite its importance in setting the time-mean rainfall pattern, orographic forcing might be less important than large-scale horizontal moisture advection in setting the daily variability of precipitation in these regions. Such control of precipitation by large-scale advection of moisture in the midtroposphere was noted over the Arabian Sea during the summer monsoon (Hunt et al. 2021) and in northern Australia during its monsoon season (Xie et al. 2010).

The regression pattern in PNG is neither cross-slope nor down-moisture-gradient. Indeed, the orographic rainband of PNG corresponds to a local maximum in lower-tropospheric specific humidity. Although we do not have a precise explanation for this pattern of wind anomalies, one may speculate that it is associated with large-scale upward motion in the South Pacific convergence zone (SPCZ), where PNG is located.

We note that moistening of the lower troposphere is not solely controlled by horizontal winds, and that any source of uplift, such as convectively coupled waves or cyclonic disturbances, will affect q_L. In this section we focused on horizontal wind control because horizontal winds dictate the strength of uplift in stationary mountain waves, and are consequently a primary factor modulating the effect of orography on q_L variations.

e. *Controls on daily precipitation variations*

To verify whether the same factors that govern lower-free-tropospheric temperature and moisture control rainfall variations, we now regress horizontal wind on daily upstream precipitation in each region (Fig. 10; upstream precipitation is defined as an average over the same boxes we previously used to define the rainbands). Enhanced rainfall is associated with some amount of upslope flow in all regions, confirming the importance of orographic mechanical forcing in influencing precipitation variability there. Deviations from pure upslope flow (especially in Vietnam, Malaysia, the Philippines, and PNG) are consistent with the wind patterns that accompany q_L variations (see Fig. 9), that is, down-moisture gradient winds. This confirms the joint control of orographic lifting and large-

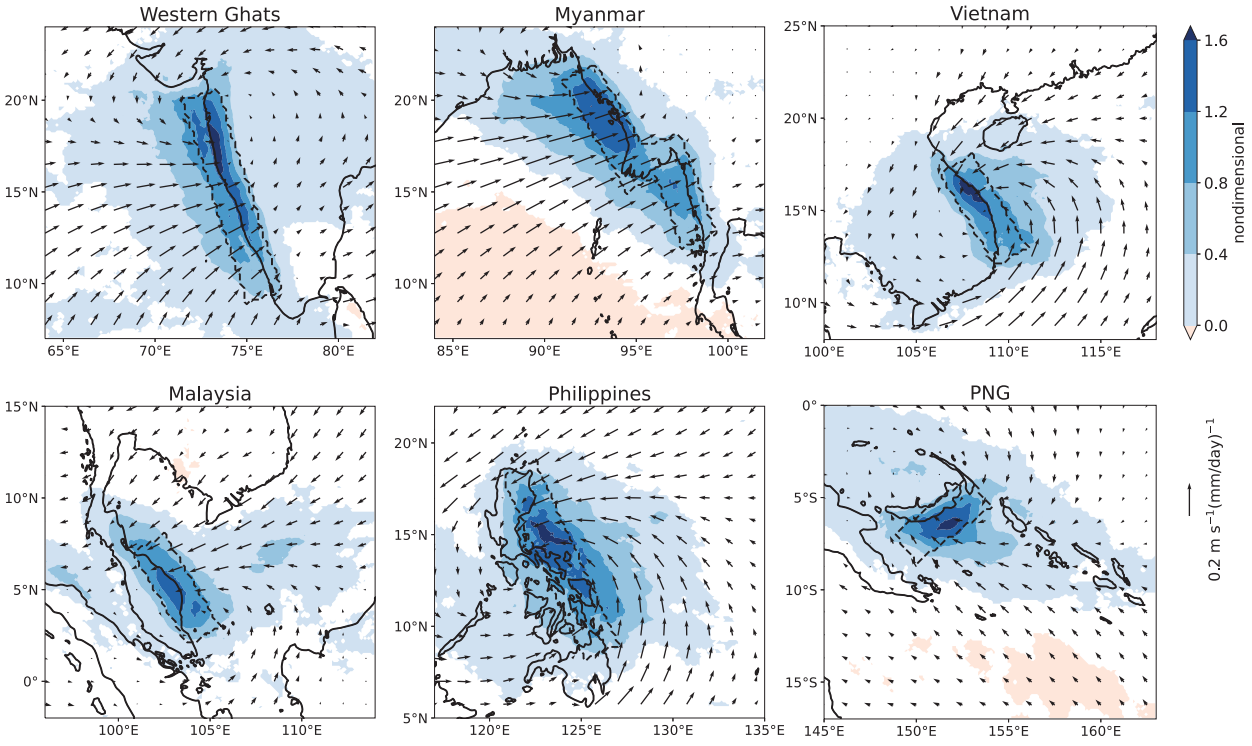

FIG. 10. Boundary layer horizontal wind regressed on precipitation averaged in the dashed boxes. The color shading shows precipitation regressed on this same index. Masked arrows and white shading indicate that the regressions do not satisfy the false discovery rate criterion with $\alpha = 0.01$.

scale moisture advection on orographic precipitation variability in the tropics.

Color shading in Fig. 10 shows precipitation regressed on this same upwind precipitation index. The existence of areas of weak positive association with the upwind rain index that are much wider than the orography indicate that orographic rainfall is partially controlled by large-scale, "background" precipitation variations. The stronger regression coefficients localized close to and preferentially upstream of the orography suggests the existence of an orographic mode of precipitation variability in each region. Patterns of positive association extend several hundred kilometers upstream of the regions used to define the rainfall index, as expected given the far-reaching influence of mechanical forcing upstream of a ridge (NB22).

5. Spatial distribution of buoyancy around orography

Strong spatial gradients are a ubiquitous characteristic of orographic rainfall. All regions in Fig. 3 exhibit a windward rainfall peak and a leeward rain shadow less than 200 km apart, with seasonal-mean precipitation rates varying from more than 15 mm day^{-1} to less than 5 mm day^{-1} on short distances. The buoyancy framework presented in section 4 naturally applies on short (hourly to daily) temporal scales, as buoyancy anomalies are consumed in a few hours (Ahmed et al. 2020). Here, we explore its potential to explain precipitation patterns on much longer time scales. Specifically, we explore whether seasonal-mean spatial features of orographic precipitation follow the spatial distribution of time-averaged buoyancy B_L.

The precipitation–B_L relationship was initially introduced as a nonlinear statistical relationship holding at short spatial and small temporal scales (Ahmed and Neelin 2018). It is statistical in the sense that a single value of B_L corresponds to a range of precipitation rates—the relationship appears when conditionally averaging precipitation. Taking time averages is thus favorable in that it eliminates the underlying stochasticity. However, averaging over a nonlinear relationship may yield a nonunique mapping between time-mean precipitation $\overline{P}$ and time-mean buoyancy $\overline{B_L}$. For example, it appears from Fig. 5 that the orographic rainband upstream of Myanmar has a narrower distribution of B_L than other regions. This suggests that $\overline{B_L}$ values in that region may be higher than in other places with comparable rain rates (e.g., upstream of the Western Ghats or PNG). Nonetheless, one might still expect a monotonic relationship between $\overline{B_L}$ and $\overline{P}$, perhaps with variations across regions.

We compute B_L from ERA5 temperature and moisture data at 0.25° and daily resolution, then average temporally over each region's rainiest season (see Table 1) for 20 years. The resulting maps are shown in Fig. 11. We note that the boundary layer top is taken as the 900-hPa level, which ignores spatial variations in boundary layer depth. Including these variations (using ERA5 estimates of boundary layer depth; not shown) does not affect the results presented here.

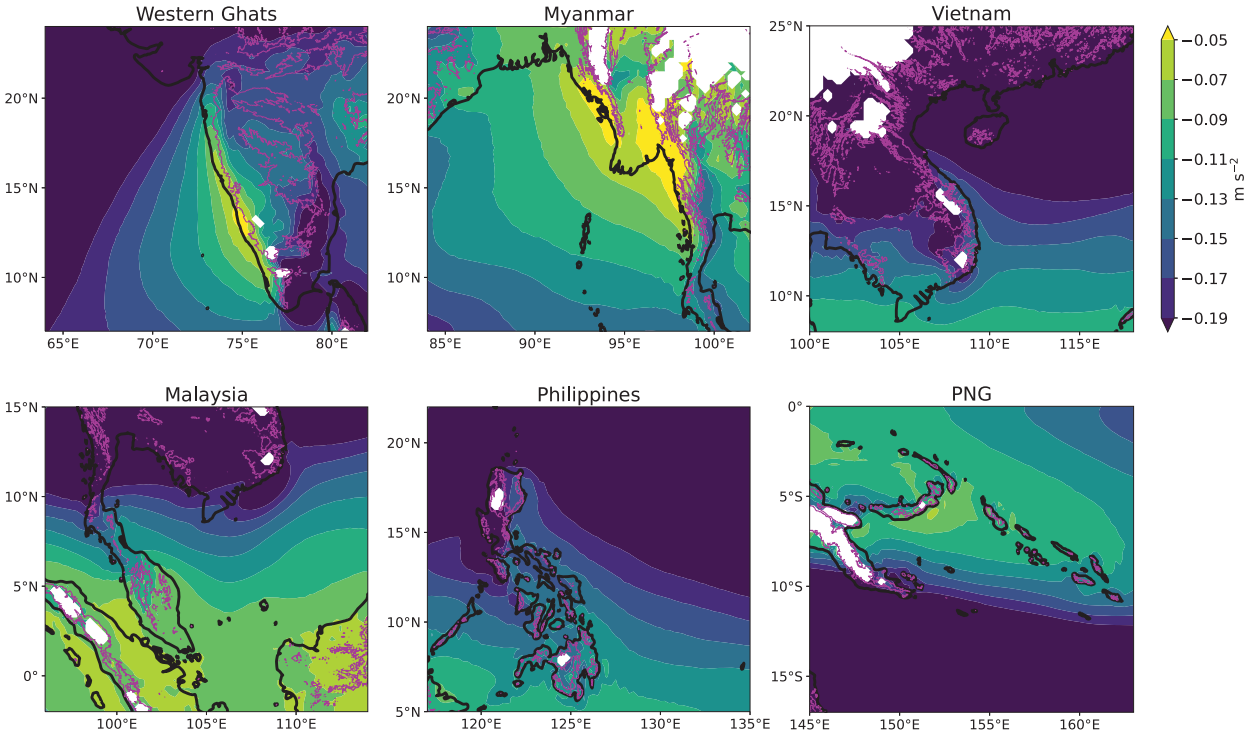

FIG. 11. Maps of seasonal-mean plume buoyancy B_L. The 500-m topography contour is shown in magenta. White shading represents undefined B_L values, wherever the surface pressure is lower than 900 hPa.

Spatial features on these maps are broadly consistent with the maps of mean precipitation in Fig. 3. A distinct peak is visible upwind of each orographic barrier, with decreased B_L values in the lee: this confirms that mechanical forcing spatially distributes precipitation in a manner consistent with its effect on the temperature and moisture fields. This effect was already noted in section 4 in the maps of time-averaged T_L and q_L (Figs. 8 and 9, where upstream cold anomalies were present in all regions, and moist anomalies in several regions). The B_L peaks are collocated with rainfall peaks (see Fig. 3) in all regions. One small exception is the easternmost B_L peak in Myanmar, which extends farther inland than the observed precipitation maximum. We note that the ERA5 precipitation distribution (not shown) follows the B_L pattern, with higher values than TRMM PR/GPM DPR inland. This may indicate that the reanalysis does not accurately represent the underlying B_L distribution there.

Except for the special case of Myanmar, rain shadows are consistent with the time-mean buoyancy distribution. Reduced values of B_L, mostly associated with a warmer and/or drier lower troposphere, are visible downstream of the mountain ranges, consistent with the expected effect of gravity wave subsidence there. In the Western Ghats and in PNG, B_L does not drop as sharply as precipitation downstream of the rainfall maximum. Once again, ERA5 precipitation (not shown) partly reflects this fact, with overestimated rainfall values especially downstream of PNG. This could mean that ERA5 underestimates the warm and dry anomalies resulting from mechanically forced subsidence there (perhaps because the topography is under-resolved). Alternatively, the B_L framework may only partially account for the suppression of precipitation in rain shadows. Convection may be affected by higher-order variations in the vertical structures of temperature and moisture, or by neglected dynamical effects (e.g., mountain lees are regions of strong wind shear).

6. A linear model for seasonal-mean tropical orographic precipitation

Section 5 suggests that the spatial organization of tropical orographic rainfall is adequately captured by the time-mean plume buoyancy distribution. However, we have yet to quantify the effect of orography on this distribution. Here, we delve further into the physical drivers through which orography influences B_L and sets the strength and location of rainfall peaks and rain shadows. We use a simple theory that solves, for any topographic shape, the time-mean temperature and moisture anomalies carried by a stationary mountain wave (including convective feedback on the moisture anomalies) to estimate the time-mean precipitation distribution. The model describes mechanically forced rainfall in tropical regions, and neglects thermal forcing and Earth's rotation. We compare its predictions with observations and with two existing theories for mechanically forced orographic rainfall.

a. Derivation

The theory we present closely follows the one developed in NB22, but extends it to two horizontal dimensions. We give

an outline of the derivation, and refer readers to that work for more details. A low-latitude domain with topography $h(x, y)$ has a constant background wind $\mathbf{u}_0 = (u_0, v_0)$ and Brunt–Väisälä frequency N. The flow is decomposed as the sum of a basic state, a "dry" mode (which carries temperature and moisture perturbations from a stationary mountain wave) and a "moist" mode (which consists of a convective response to these perturbations). The dry mode influences the moist mode by altering convective heating and moistening, which are parameterized as functions of lower-tropospheric temperature and moisture following the B_L framework, but the moist mode does not affect the dry mode. This simplifying assumption allows for analytical tractability, and was tested in NB22; idealized simulations showed that the moist mode does reduce the temperature perturbations carried by the dry mode, but that this effect is of second-order importance. In this section only, temperature and moisture are in energy units (compared to the previous sections, they are multiplied by c_p), for consistency with NB22.

Steady-state thermodynamic and moisture equations for the moist mode read as follows:

$$\mathbf{u}_0 \cdot \nabla T_m + \omega_m \frac{ds_0}{dp} = Q_c - R, \tag{7a}$$

$$\mathbf{u}_0 \cdot \nabla q_m + \omega_m \frac{dq_0}{dp} = Q_q + E, \tag{7b}$$

where $s_0(p)$ and $q_0(p)$ are the background dry static energy profile and moisture profile (in energy units). The terms Q_c and Q_q denote convective heating and moistening, while R and E are radiative cooling and surface evaporation rates. Also, ω is the pressure velocity, and the subscript m is used for moist mode quantities (we will similarly use a subscript d for dry mode properties), so T_m and q_m are, respectively, the moist mode temperature and moisture perturbations.

We use the weak temperature gradient approximation for the moist mode, which implies that T_m is horizontally uniform. This allows us to set $T_m = 0$: one can add any horizontally uniform nonzero $T_m(p)$ to the reference profile $T_0(p)$, hence resulting in $T_m = 0$. Truncating the vertical velocity profile as $\omega_m(x, y, p) = \omega_1(x, y)\Omega(p)$, where Ω is a fixed vertical profile, and vertically averaging over the depth of the troposphere yields

$$-\omega_1 M_s = \langle Q_c \rangle - \langle R \rangle, \tag{8a}$$

$$\mathbf{u}_0 \cdot \nabla \langle q_m \rangle + \omega_1 M_q = \langle Q_q \rangle + \langle E \rangle, \tag{8b}$$

where $M_s = -\langle \Omega \partial s_0/\partial p \rangle$, $M_q = \langle \Omega \partial q_0/\partial p \rangle$, and $\langle \cdot \rangle$ denotes a vertical average in pressure coordinates. $M = M_s - M_q$ is known as the gross moist stability, and M/M_s as the normalized gross moist stability (NGMS; Raymond et al. 2009).

Following Ahmed et al. (2020), the precipitation–B_L relationship is linearized (and boundary layer θ_e is assumed constant), yielding

$$\langle Q_c \rangle = \frac{q'_L}{\tau_q} - \frac{T'_L}{\tau_T} = \frac{q_{dL} + q_{mL}}{\tau_q} - \frac{T_{dL}}{\tau_T}, \tag{9}$$

where q_{dL} and q_{mL} are lower-free-tropospheric moisture perturbations carried by the dry and moist modes, T_{dL} is the dry mode temperature perturbation (recall $T_m = 0$), and the convective time scales τ_T and τ_q are constants appearing from the linearization. For seasonal-mean rainfall, these are taken as $\tau_T = 7.5$ h and $\tau_q = 27.5$ h, a factor 2.5 higher than their values when used to represent precipitation at the hourly scale. Because the vertical structure of moisture perturbations is horizontally uniform, q_{mL} and $\langle q_m \rangle$ are proportional to each other; we therefore define an adjustment time scale for vertically averaged moisture, $\tilde{\tau}_q = 0.6\tau_q$ such that $q_{mL}/\tau_q = \langle q_m \rangle/\tilde{\tau}_q$.

We now use conservation of energy to relate convective heating, moistening, and precipitation by

$$\langle Q_c \rangle = -\langle Q_q \rangle = \frac{\rho_w L_v g}{p_T} P, \tag{10}$$

where $p_T = 800$ hPa is the depth of the troposphere and $\rho_w = 1000$ kg m^{-3} is the density of water. The first factor on the right-hand side converts a precipitation rate (in m s^{-1} or mm day^{-1}) into a convective heating rate (in J kg^{-1} s^{-1}). We henceforth define $\beta = p_T/(\rho_w L_v g)$. Using this definition and combining (8a), (8b), (9), and (10), we derive an equation for P:

$$\mathbf{u}_0 \cdot \nabla P + \frac{\mathrm{NGMS}}{\tilde{\tau}_q}(P - P_0) = \beta \mathbf{u}_0 \cdot \nabla \left(\frac{q_{dL}}{\tau_q} - \frac{T_{dL}}{\tau_T} \right), \tag{11}$$

where $P_0 = \beta[(M_s \langle E \rangle - M_q \langle R \rangle)/M]$ is a background rain rate. The right-hand side of Eq. (11) represents a forcing of convection by the dry mode. The second term on the left-hand side represents convective relaxation: precipitation forced by the cool and moist perturbations of the dry mode dries the lower free troposphere, which in turn relaxes rainfall back toward the background rate P_0. The reverse process happens when precipitation is suppressed by warm and dry perturbations. This process happens on a length scale $L_q = \tilde{\tau}_q |\mathbf{u}_0|/\mathrm{NGMS}$. We note that this framework is suitable for various vertical structures of convection, and that changes in the vertical structure $\Omega(p)$ only affect the solutions through the NGMS. Remarkably, solutions can be obtained with negative NGMS (which typically results from bottom-heavy vertical motion profiles; e.g., Back and Bretherton 2006). In these cases, convection amplifies (rather than damps) the precipitation perturbation forced by the dry mode.

Solving for T_{dL} and q_{dL} using mountain wave theory allows us to map a given topographic shape to the associated precipitation distribution using a Fourier transform. In the dry mode, moisture is conserved and there are no diabatic processes. Hence, horizontal advection terms are balanced by vertical advection:

$$\mathbf{u}_0 \cdot \nabla \left(\frac{q_{dL}}{\tau_q} - \frac{T_{dL}}{\tau_T} \right) = w_{dL} \left(\frac{1}{\tau_T} \frac{ds_0}{dz} - \frac{1}{\tau_q} \frac{dq_0}{dz} \right), \tag{12}$$

where w_{dL} is the vertical velocity of the dry mode (we use height coordinates in the spirit of linear mountain wave theory). We define

$$\chi = \beta \left(\frac{1}{\tau_T} \frac{ds_0}{dz} - \frac{1}{\tau_q} \frac{dq_0}{dz} \right) \tag{13}$$

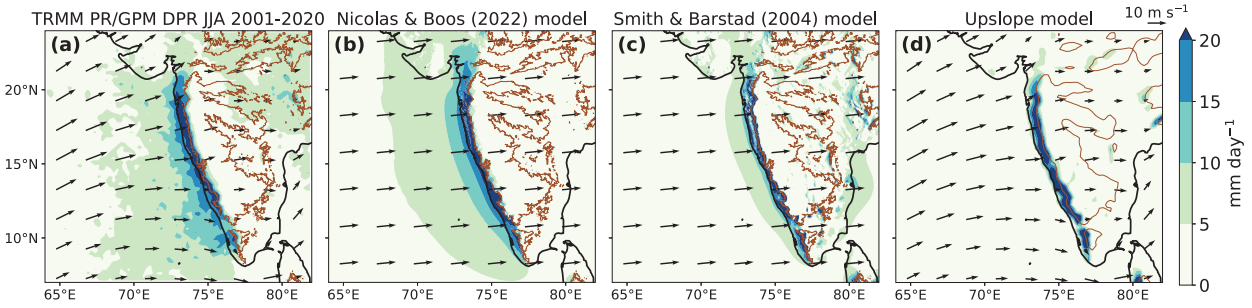

FIG. 12. Maps of mean precipitation in the Western Ghats. (a) Observations (TRMM PR and GPM DPR), (b) Nicolas and Boos (2022) theory, (c) Smith and Barstad (2004) theory, and (d) upslope model ($\mathbf{IVT} \cdot \nabla h/H_{\text{sat}}$).

and substitute (12) into (11), which becomes (defining $P' = P - P_0$)

$$\mathbf{u}_0 \cdot \nabla P' + \frac{\text{NGMS}}{\tilde{\tau}_q} P' = \chi w_{dL}. \tag{14}$$

Here, w_{dL} is given by linear mountain wave theory, in two horizontal dimensions under the Boussinesq approximation, by (Smith 1979)

$$\hat{w}_d(k_x, k_y, z) = i\sigma\hat{h}(k_x, k_y)\exp[im(k_x, k_y)z], \tag{15}$$

where k_x and k_y are the horizontal wavenumbers, hats denote Fourier transforms, $\sigma = k_x u_0 + k_y v_0$, and z is the vertical coordinate. Defining $K^2 = k_x^2 + k_y^2$, the vertical wavenumber $m(k_x, k_y)$ is

$$m = \begin{cases} \text{sgn}(\sigma)\sqrt{K^2\left(\dfrac{N^2}{\sigma^2} - 1\right)}, & \text{if } \sigma^2 < N^2 \\ i\sqrt{K^2\left(1 - \dfrac{N^2}{\sigma^2}\right)}, & \text{if } \sigma^2 > N^2 \end{cases}. \tag{16}$$

Fourier-transforming (14) and using (15) gives a closed expression for the Fourier-transformed precipitation anomaly $\hat{P}'$:

$$\hat{P}'(k_x, k_y) = \frac{i\sigma\chi}{i\sigma + \dfrac{\text{NGMS}}{\tilde{\tau}_q}} \hat{h}(k_x, k_y)\{\exp[im(k_x, k_y)z]\}_L. \tag{17}$$

The main controlling parameters are topography $h(x)$, background wind u_0, stratification N, and a background moisture lapse rate. We note that in this model, the lower troposphere is defined between 1 and 3 km above sea level. With this choice, mountain waves that have small vertical wavelengths may have positive temperature anomalies and negative moisture anomalies in the lower troposphere upstream of topography, and the model predicts small or negative rainfall enhancement in these cases. For $N \simeq 0.01$ s^{-1}, this happens when $U < 8$ m s^{-1}; the model is not recommended for use below this wind speed without some attention to redefining the vertical span of the lower troposphere, as well as taking thermal forcing into account. We now apply this model to the real-world tropics.

b. Comparing observed and modeled rainfall distributions

The ingredients comprising the above theory (weak temperature gradient approximation, quasiequilibrium precipitation closure) make it especially suited to tropical regions. SB04 developed a model of mechanically forced orographic rainfall for convectively stable flows that has been used to represent midlatitude orographic precipitation. While SB04 did not intend their model for use in tropical regions, it is arguably the most widely used theoretical model of orographic precipitation, and as such provides a point of comparison with the present theory. Their model assumes that condensation results from ascent in a saturated atmosphere [see (1)]. Unlike the upslope model, however, vertical motion is computed using linear mountain wave theory, and the effects of finite hydrometeor growth times and downwind advection are parameterized. The fundamental difference between the models of SB04 and NB22 is the mechanism linking mountain waves to precipitation: in the former, rain is associated with the ascent rate w, while in the latter, it is associated with vertical displacement of the lower free troposphere from a background state. This results in shorter length scales for the upstream enhancement of rainfall and rain shadows in SB04's model. This can be understood qualitatively with the idealized topographic profile used in the appendix, which decays as $h(x) \propto x^{-2}$ upstream of the mountain; while the vertical displacement should scale approximately like $h(x)$, the vertical motion will scale as dh/dx and thus have a faster decay rate of x^{-3}.

We compare observed and modeled seasonal-mean rainfall maps[4] in the Western Ghats in Fig. 12. Both the SB04 and NB22 models use a uniform static stability; we choose $N = 0.01$ s^{-1}, which corresponds to a lapse rate of 6.5 K km^{-1}, close to the free-tropospheric lapse rate in the Ghats. Because tropical lapse rates are steeper than moist adiabats, we do not use SB04's "moist static stability" (which is negative in all regions) to calculate stationary mountain waves in the SB04 model. SB04 further require a moist adiabatic lapse rate, taken as $\Gamma_m = 4.3$ K km^{-1} (corresponding to a lower-tropospheric average for a surface temperature of 300 K), and hydrometeor

[4] For both models, the domain shown in Fig. 12 is padded to a square domain of side length 7500 km, with topography smoothed down to zero elevation 100 km outside of the main domain.

TABLE 4. Parameters used in the precipitation models of Smith and Barstad (2004) and Nicolas and Boos (2022).

Region name	u_0 (m s^{-1})	v_0 (m s^{-1})	P_0 (mm day^{-1})
Western Ghats	10	1	3
Myanmar	8	8	6
Vietnam	−7	−5	4
Malaysia	−7	−5	10
Philippines	−8.5	−3	4
PNG	−7.5	5.5	3

growth and fallout times, both taken as 1000 s (as suggested in SB04). To account for nonprecipitating times, the SB04 perturbation precipitation rates are divided by the factor 2.5, chosen in NB22 to fit peak rain rates from SB04 to convection-permitting simulations. For the NB22 model, we choose a lower-tropospheric moisture lapse rate of −8 K km^{-1} and NGMS = 0.2, representative of all the regions studied herein. Finally, the background wind and precipitation rate are given in Table 4, chosen to match upstream values from ERA5 and TRMM PR/GPM DPR. Both theories (Figs. 12b,c) produce an upstream precipitation peak that is commensurate with observations (around 20 mm day^{-1}). As explained above, precipitation enhancement happens much closer to the ridge in the SB04 model, which fails to account for high precipitation rates over the Arabian Sea upstream of the Western Ghats. It also predicts a second rainfall peak downstream, by the eastern coast of India, associated with vertical motion predicted by linear mountain wave theory there. This is unlike the NB22 model, which features an extensive rain shadow. Although central and northeastern India do receive precipitation during summer (Fig. 12a), this is commonly thought to arise from the dynamics of synoptic-scale disturbances such as monsoon depressions (Sikka 1977) rather than mountain wave ascent downstream of the Indian topography.

For reference, Fig. 12d shows precipitation from the upslope model [Eq. (2)]. We convert the condensation rate into a precipitation rate using an efficiency factor $\epsilon = 0.25$, chosen to match peak precipitation rates in the Ghats. We use 0.25° × 0.25° topography, as higher resolutions lead to unrealistic small-scale features in this model. Because it only predicts precipitation above mountain slopes, it does not account for any upstream rainfall enhancement. By design, this model predicts peak rainfall to occur on the steepest upstream slopes, and does capture a large part of the observed peak directly above the windward Ghats.

We extend this analysis to all regions, and show cross-sectional averages of the observed and modeled mean precipitation rates in Fig. 13. The insets show the direction and width of the cross sections, which were chosen normal to topography and following the prevailing wind direction. Background wind speeds and precipitation rates are listed in Table 4. With the fixed precipitation efficiency $\epsilon = 0.25$ that produced a

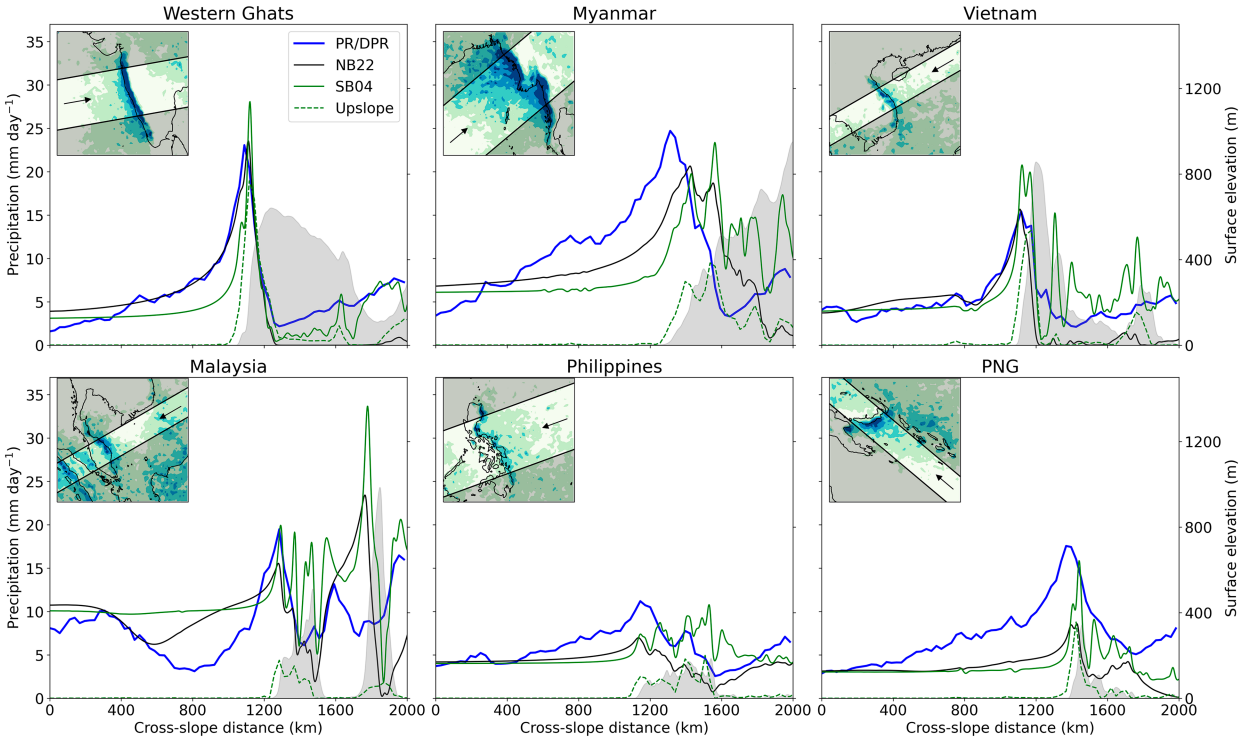

FIG. 13. Cross sections of observed and modeled precipitation in all regions, along the direction of the seasonal-mean wind. The insets show the orientation and width of the areas used to define cross sections (the background shows mean observed precipitation from TRMM PR and GPM DPR, as in Fig. 3). The gray shadings represent topography. The dark blue lines are observed mean precipitation during each region's rainiest season. Other lines show precipitation from the Nicolas and Boos (2022) theory (black), the Smith and Barstad (2004) theory (solid green), and the upslope model (dashed green).

match to the peak precipitation magnitude in the Western Ghats, the upslope model underestimates peak precipitation rates in nearly all other regions. Thus, in addition to missing the upstream enhancement of precipitation, this model requires region-specific tuning to yield accurate peak rainfall rates. The SB04 and NB22 models produce similar peak rain rates in all regions, differing primarily in the upstream extent of the orographic rainfall enhancement and in the leeside precipitation rates. The NB22 model accurately predicts the rainfall enhancement upstream of certain regions (especially the Western Ghats and Vietnam), while the SB04 model predicts rainfall to pick up much closer to the topography, at odds with observations. The description of orographic rainfall as the result of forced temperature and moisture perturbations in a lower-tropospheric quasi-equilibrium state is thus consistent with observations there. In other regions (most notably the Philippines and PNG), both models greatly underestimate precipitation rates compared to observations. In the NB22 model, this failure results from an underestimation of the moisture anomaly q_L' (not shown). We speculate that positive q_L perturbations are not only the result of orographic lifting in these regions, and that climatological mean large-scale ascent, forced by nonorographic factors, plays a key role in producing the observed rainfall patterns. The fact that PNG is located within the SPCZ is consistent with this hypothesis.

Differences between observed and modeled precipitation rates are also apparent downstream of the mountain ranges. The NB22 model seems to strongly overestimate the drying effect of orography there. The main reason for this flaw is that the model assumes a time-independent background wind, which leads the lee of mountains to be persistently warm and dry. In reality, some days exhibit reversed flow or have a stronger along-slope component, creating more favorable conditions for convection in the lee. Additionally, synoptic disturbances (such as monsoon depressions downstream of the Indian subcontinent) may occasionally propagate into these regions, contributing to small positive seasonal-average precipitation there. As explained above in the case of the Western Ghats, the SB04 model predicts higher leeside precipitation rates, because linear mountain wave solutions produce ascent there. This leads to localized downstream precipitation peaks that are not seen in observations.

7. Discussion and conclusions

Here we investigated the spatial and temporal distribution of mechanically forced orographic rainfall in six tropical regions. We showed that a buoyancy proxy, evaluated from reanalysis data, captures many aspects of both daily variations and the seasonal-mean spatial distribution of rainfall in all regions. In this framework, the interaction of orography with the background wind creates temperature and moisture anomalies in the lower troposphere, affecting the buoyancy of convective plumes and thereby controlling precipitation.

This work confirms the important role of lower-free-tropospheric moisture (q_L) in controlling temporal variations in orographic convection. In the absence of background horizontal moisture gradients, q_L variations would be fully controlled by orographic uplift, hence primarily by the cross-slope wind speed. The presence of large-scale q_L gradients leads alternate directions of wind anomalies to favor rainfall in some regions, namely down-moisture-gradient winds. These results indicate that mechanical forcing only exerts a partial control on rainfall variations in the regions studied. Together, these findings establish a new view of tropical orographic precipitation being enhanced by moistening of the lower troposphere due to both upslope flow and large-scale horizontal advection.

Despite the nonlinear relationship between plume buoyancy B_L and precipitation, time-averaged B_L captures many spatial features of observed seasonal-mean precipitation maps. Discrepancies appear in the rain shadows, where B_L (as estimated from a reanalysis) overestimates precipitation. This points to a possible limitation of the present framework, in which convective dynamics are assumed identical over oceans and in mountains, with mountains only affecting plume buoyancy. Nevertheless, our goal here is to provide a first-order understanding of the mechanisms governing tropical orographic precipitation. We recognize that this approach neglects the influence of some aspects of orographic dynamics, such as strong wind shears and gravity wave breaking, on convection.

We present a linear theory that predicts the time-mean rainfall distribution for arbitrary 2D topography and uniform wind. It quantifies the lower-tropospheric temperature and moisture perturbations caused by stationary mountain waves, and takes into account the feedback of convection on the moisture distribution. The theory accurately predicts upstream rainfall in some regions, especially the Western Ghats and Vietnam. In other regions (mainly the Philippines and PNG), it yields weaker peak rainfall than observations. It is likely that mechanical forcing alone cannot explain the strong rainbands observed there. The presence of climatological-mean ascent, due to nonorographic factors (such as the SPCZ in PNG), plays a key role in setting the lower-tropospheric moisture gradients, hence the rainfall patterns, in these regions.

The theoretical model presented herein only describes mechanically forced rainfall in tropical regions. As such, it is expected to work with small nondimensional mountain heights and sufficiently strong winds (we recommend its use for wind speeds of at least 8 m s^{-1}). The model does not describe thermal forcing (expected to dominate in weak horizontal winds and/or large nondimensional mountain heights), nor is it suitable for moist convectively stable ascent cases, more common in midlatitude winter. Our use of the weak temperature gradient approximation for the moist mode, and neglect of the Coriolis parameter, may make it most appropriate for the tropics.

One other limitation of this study is that it does not investigate the vertical structure of convection, which past work has shown varies in tropical orographic regions (Kumar and Bhat 2017; Shige and Kummerow 2016). However, we have demonstrated that the buoyancy framework accurately characterizes precipitation in the six regions studied, irrespective of the mean depth of convection. Furthermore, the theoretical model assumes a fixed but arbitrary vertical structure of

upward motion, and is thus applicable to a wide range of tropical regions (perhaps with modification of the coefficients that depend on the vertical structure of ascent). However, the buoyancy framework might not apply in trade wind regions, which are characterized by very shallow convection beneath an inversion layer [for a study of orographic precipitation in the trades, see Kirshbaum and Smith (2009)].

This work suggests that two ingredients are needed to accurately represent tropical orographic convection: free-tropospheric temperature and moisture anomalies generated by flow over terrain, and the dependence of convection on those thermodynamic perturbations. This implies that a coarse-resolution model with a good convective parameterization may perform well around orography, as long as the magnitude of lower-tropospheric vertical displacement over the terrain is captured. We hope that future work will investigate the representation of tropical orographic rainfall in climate models under this lens.

Acknowledgments. This material is based on work supported by the U.S. Department of Energy, Office of Science, Office of Biological and Environmental Research, Climate and Environmental Sciences Division, Regional and Global Model Analysis Program, under Award DE-SC0019367. It used resources of the National Energy Research Scientific Computing Center (NERSC), which is a DOE Office of Science User Facility.

Data availability statement. The code containing linear precipitation models, the code used in producing the figures, and the processed ERA5 and precipitation data are archived at Zenodo (Nicolas 2023).

APPENDIX

Lower-Tropospheric Temperature and Moisture Perturbations Forced by an Idealized Ridge

We consider an infinite two-dimensional (x–z) domain whose surface height is

$$h(x) = h_m \frac{l_0^2}{x^2 + l_0^2}, \tag{A1}$$

where l_0 is the mountain half-width and h_m is the maximum height. This topographic profile, commonly known as a Witch of Agnesi, has a convenient Fourier transform, which renders the treatment of mountain wave solutions analytically tractable. The background horizontal wind speed U and static stability N are supposed uniform. We now estimate mechanically forced temperature perturbations using linear mountain wave theory, which is approximately valid under the assumption of small nondimensional mountain height Nh_m/U. Queney (1948) gives an analytical solution for $\zeta(x, z)$, the vertical displacement at x of a streamline originating upstream at z:

$$\zeta(x, z) = h_m \frac{\cos(Nz/U) l_0^2 - \sin(Nz/U) l_0 x}{x^2 + l_0^2}. \tag{A2}$$

This expression is valid when $l_0 N/U \gg 1$, which is largely satisfied with a half-width $l_0 \simeq 100$ km, $U \simeq 10$ m s^{-1}, and $N \simeq 0.01$ s^{-1}. With uniform static stability, and in the absence of diabatic processes, a parcel lifted by ζ experiences a cooling of magnitude $\zeta ds_0/dz$. Thus, the lower-free-tropospheric temperature perturbation is

$$T'_L(x) = -h_m \frac{ds_0}{dz} \frac{\alpha_c l_0^2 - \alpha_s l_0 x}{x^2 + l_0^2}, \tag{A3}$$

where $\alpha_c = [\cos(Nz/U)]_L$, $\alpha_s = [\sin(Nz/U)]_L$, and $[\cdot]_L$ denotes a lower-tropospheric average. $s_0(z)$ is the background dry static energy profile profile (divided by c_p). Minimizing (A3) gives the peak lower-tropospheric temperature perturbation:

$$T'_{L,\max} = -h_m \frac{ds_0}{dz} \left(\sqrt{\alpha_c^2 + \alpha_s^2} + \alpha_c \right), \tag{A4}$$

Evaluating $\partial T'_{L,\max}/\partial U$ with a 1-km high mountain and $N = 0.01$ s^{-1} gives (5).

The peak moisture perturbation is given by the same expression as (A4), replacing ds_0/dz with dq_0/dz [where $q_0(z)$ is a background moisture profile]. Using a lower-free-tropospheric moisture lapse rate representative of our regions (8 K km^{-1}), we obtain (6).

REFERENCES

Ahmed, F., and J. D. Neelin, 2018: Reverse engineering the tropical precipitation–buoyancy relationship. *J. Atmos. Sci.*, **75**, 1587–1608, https://doi.org/10.1175/JAS-D-17-0333.1.

——, Á. F. Adames, and J. D. Neelin, 2020: Deep convective adjustment of temperature and moisture. *J. Atmos. Sci.*, **77**, 2163–2186, https://doi.org/10.1175/JAS-D-19-0227.1.

Amante, C., and B. Eakins, 2009: ETOPO1 1 arc-minute global relief model: Procedures, data sources and analysis. NOAA Tech. Memo. NESDIS NGDC-24, 25 pp., https://www.ngdc.noaa.gov/mgg/global/relief/ETOPO1/docs/ETOPO1.pdf.

Anber, U., S. Wang, and A. Sobel, 2014: Response of atmospheric convection to vertical wind shear: Cloud-system-resolving simulations with parameterized large-scale circulation. Part I: Specified radiative cooling. *J. Atmos. Sci.*, **71**, 2976–2993, https://doi.org/10.1175/JAS-D-13-0320.1.

Aoki, S., and S. Shige, 2024: Control of low-level wind on the diurnal cycle of tropical coastal precipitation. *J. Climate*, **37**, 229–247, https://doi.org/10.1175/JCLI-D-23-0180.1.

Back, L. E., and C. S. Bretherton, 2006: Geographic variability in the export of moist static energy and vertical motion profiles in the tropical Pacific. *Geophys. Res. Lett.*, **33**, 2006GL026672, https://doi.org/10.1029/2006GL026672.

Bagtasa, G., 2020: Influence of Madden–Julian oscillation on the intraseasonal variability of summer and winter monsoon rainfall in the Philippines. *J. Climate*, **33**, 9581–9594, https://doi.org/10.1175/JCLI-D-20-0305.1.

Biasutti, M., S. E. Yuter, C. D. Burleyson, and A. H. Sobel, 2012: Very high resolution rainfall patterns measured by TRMM precipitation radar: Seasonal and diurnal cycles. *Climate Dyn.*, **39**, 239–258, https://doi.org/10.1007/s00382-011-1146-6.

Bretherton, C. S., M. E. Peters, and L. E. Back, 2004: Relationships between water vapor path and precipitation over the tropical oceans. *J. Climate*, **17**, 1517–1528, https://doi.org/10.1175/1520-0442(2004)017<1517:RBWVPA>2.0.CO;2.

Chang, C.-P., Z. Wang, J. McBride, and C.-H. Liu, 2005: Annual cycle of Southeast Asia—Maritime Continent rainfall and the asymmetric monsoon transition. *J. Climate*, **18**, 287–301, https://doi.org/10.1175/JCLI-3257.1.

Chase, R. J., and H. A. Syed, 2022: dopplerchase/DRpy: First major release, version v1.0.0. Zenodo, accessed 1 March 2023, https://doi.org/10.5281/zenodo.7259561.

Chen, T.-C., J.-D. Tsay, M.-C. Yen, and J. Matsumoto, 2012: Interannual variation of the late fall rainfall in central Vietnam. *J. Climate*, **25**, 392–413, https://doi.org/10.1175/JCLI-D-11-00068.1.

——, ——, ——, and ——, 2013: The winter rainfall of Malaysia. *J. Climate*, **26**, 936–958, https://doi.org/10.1175/JCLI-D-12-00174.1.

Derbyshire, S. H., I. Beau, P. Bechtold, J.-Y. Grandpeix, J.-M. Piriou, J.-L. Redelsperger, and P. M. M. Soares, 2004: Sensitivity of moist convection to environmental humidity. *Quart. J. Roy. Meteor. Soc.*, **130**, 3055–3079, https://doi.org/10.1256/qj.03.130.

Emanuel, K. A., J. D. Neelin, and C. S. Bretherton, 1994: On large-scale circulations in convecting atmospheres. *Quart. J. Roy. Meteor. Soc.*, **120**, 1111–1143, https://doi.org/10.1002/qj.49712051902.

Espinoza, J. C., S. Chavez, J. Ronchail, C. Junquas, K. Takahashi, and W. Lavado, 2015: Rainfall hotspots over the southern tropical Andes: Spatial distribution, rainfall intensity, and relations with large-scale atmospheric circulation. *Water Resour. Res.*, **51**, 3459–3475, https://doi.org/10.1002/2014WR016273.

Grossman, R. L., and D. R. Durran, 1984: Interaction of low-level flow with the Western Ghat Mountains and offshore convection in the summer monsoon. *Mon. Wea. Rev.*, **112**, 652–672, https://doi.org/10.1175/1520-0493(1984)112<0652:IOLLFW>2.0.CO;2.

Hersbach, H., and Coauthors, 2018: ERA5 hourly data on pressure levels from 1959 to present. Copernicus Climate Change Service (C3S) Climate Data Store (CDS), accessed 24 September 2021, https://doi.org/10.24381/cds.bd0915c6.

——, and Coauthors, 2020: The ERA5 global reanalysis. *Quart. J. Roy. Meteor. Soc.*, **146**, 1999–2049, https://doi.org/10.1002/qj.3803.

Houze, R. A., Jr., 2012: Orographic effects on precipitating clouds. *Rev. Geophys.*, **50**, RG1001, https://doi.org/10.1029/2011RG000365.

——, K. L. Rasmussen, M. D. Zuluaga, and S. R. Brodzik, 2015: The variable nature of convection in the tropics and subtropics: A legacy of 16 years of the Tropical Rainfall Measuring Mission satellite. *Rev. Geophys.*, **53**, 994–1021, https://doi.org/10.1002/2015RG000488.

Huffman, G. J., E. T. Stocker, D. T. Bolvin, E. J. Nelkin, and J. Tan, 2019: GPM IMERG final precipitation L3 1 day 0.1 degree × 0.1 degree V06. Goddard Earth Sciences Data and Information Services Center (GES DISC), accessed 11 November 2021, https://doi.org/10.5067/GPM/IMERGDF/DAY/06.

Hunt, K. M. R., A. G. Turner, T. H. M. Stein, J. K. Fletcher, and R. K. H. Schiemann, 2021: Modes of coastal precipitation over southwest India and their relationship with intraseasonal variability. *Quart. J. Roy. Meteor. Soc.*, **147**, 181–201, https://doi.org/10.1002/qj.3913.

Iguchi, T., and R. Meneghini, 2021: GPM DPR precipitation profile 1 month 0.25 degree × 0.25 degree V07. Goddard Earth Sciences Data and Information Services Center (GES DISC), accessed 10 September 2023, https://doi.org/10.5067/GPM/DPR/3A-MONTH/07.

Johnston, B. R., W. J. Randel, and J. P. Sjoberg, 2021: Evaluation of tropospheric moisture characteristics among COSMIC-2, ERA5 and MERRA-2 in the tropics and subtropics. *Remote Sens.*, **13**, 880, https://doi.org/10.3390/rs13050880.

Kirshbaum, D. J., and R. B. Smith, 2008: Temperature and moist-stability effects on midlatitude orographic precipitation. *Quart. J. Roy. Meteor. Soc.*, **134**, 1183–1199, https://doi.org/10.1002/qj.274.

——, and ——, 2009: Orographic precipitation in the tropics: Large-eddy simulations and theory. *J. Atmos. Sci.*, **66**, 2559–2578, https://doi.org/10.1175/2009JAS2990.1.

——, B. Adler, N. Kalthoff, C. Barthlott, and S. Serafin, 2018: Moist orographic convection: Physical mechanisms and links to surface-exchange processes. *Atmosphere*, **9**, 80, https://doi.org/10.3390/atmos9030080.

Kumar, S., and G. S. Bhat, 2017: Vertical structure of orographic precipitating clouds observed over South Asia during summer monsoon season. *J. Earth Syst. Sci.*, **126**, 114, https://doi.org/10.1007/s12040-017-0897-9.

Li, D., and Coauthors, 2022: High Mountain Asia hydropower systems threatened by climate-driven landscape instability. *Nat. Geosci.*, **15**, 520–530, https://doi.org/10.1038/s41561-022-00953-y.

Lindzen, R. S., and S. Nigam, 1987: On the role of sea surface temperature gradients in forcing low-level winds and convergence in the tropics. *J. Atmos. Sci.*, **44**, 2418–2436, https://doi.org/10.1175/1520-0469(1987)044<2418:OTROSS>2.0.CO;2.

Lyon, B., H. Cristi, E. R. Verceles, F. D. Hilario, and R. Abastillas, 2006: Seasonal reversal of the ENSO rainfall signal in the Philippines. *Geophys. Res. Lett.*, **33**, L24710, https://doi.org/10.1029/2006GL028182.

National Geophysical Data Center, 2011: ETOPO1, Global 1 arc-minute ocean depth and land elevation from the US National Geophysical Data Center (NGDC). NCAR, accessed 10 September 2022, https://doi.org/10.5065/D69Z92Z5.

Nelson, T. C., J. Marquis, J. M. Peters, and K. Friedrich, 2022: Environmental controls on simulated deep moist convection initiation occurring during RELAMPAGO-CACTI. *J. Atmos. Sci.*, **79**, 1941–1964, https://doi.org/10.1175/JAS-D-21-0226.1.

Nicolas, Q., 2023: qnicolas/tropicalOrographicRegions: Revisions stage for Nicolas & Boos—Understanding the spatiotemporal variability of tropical orographic rainfall using convective plume buoyancy, version v1.0.0. Zenodo, accessed 27 October 2023, https://doi.org/10.5281/zenodo.10048884.

——, and W. R. Boos, 2022: A theory for the response of tropical moist convection to mechanical orographic forcing. *J. Atmos. Sci.*, **79**, 1761–1779, https://doi.org/10.1175/JAS-D-21-0218.1.

Nugent, A. D., R. B. Smith, and J. R. Minder, 2014: Wind speed control of tropical orographic convection. *J. Atmos. Sci.*, **71**, 2695–2712, https://doi.org/10.1175/JAS-D-13-0399.1.

Ogura, Y., and M. Yoshizaki, 1988: Numerical study of orographic-convective precipitation over the eastern Arabian Sea and the Ghat Mountains during the summer monsoon. *J. Atmos. Sci.*, **45**, 2097–2122, https://doi.org/10.1175/1520-0469(1988)045<2097:NSOOCP>2.0.CO;2.

Oouchi, K., A. T. Noda, M. Satoh, B. Wang, S.-P. Xie, H. G. Takahashi, and T. Yasunari, 2009: Asian summer monsoon simulated by a global cloud-system-resolving model: Diurnal to

intra-seasonal variability. *Geophys. Res. Lett.*, **36**, L11815, https://doi.org/10.1029/2009GL038271.

Peters, J. M., H. Morrison, T. C. Nelson, J. N. Marquis, J. P. Mulholland, and C. J. Nowotarski, 2022a: The influence of shear on deep convection initiation. Part I: Theory. *J. Atmos. Sci.*, **79**, 1669–1690, https://doi.org/10.1175/JAS-D-21-0145.1.

——, ——, ——, ——, ——, and ——, 2022b: The influence of shear on deep convection initiation. Part II: Simulations. *J. Atmos. Sci.*, **79**, 1691–1711, https://doi.org/10.1175/JAS-D-21-0144.1.

Pradhan, R. K., and Coauthors, 2022: Review of GPM IMERG performance: A global perspective. *Remote Sens. Environ.*, **268**, 112754, https://doi.org/10.1016/j.rse.2021.112754.

Queney, P., 1948: The problem of air flow over mountains: A summary of theoretical studies. *Bull. Amer. Meteor. Soc.*, **29**, 16–26, https://doi.org/10.1175/1520-0477-29.1.16.

Ramesh, N., Q. Nicolas, and W. R. Boos, 2021: The globally coherent pattern of autumn monsoon precipitation. *J. Climate*, **34**, 5687–5705, https://doi.org/10.1175/JCLI-D-20-0740.1.

Raymond, D. J., Ž. Fuchs, S. Gjorgjievska, and S. Sessions, 2015: Balanced dynamics and convection in the tropical troposphere. *J. Adv. Model. Earth Syst.*, **7**, 1093–1116, https://doi.org/10.1002/2015MS000467.

——, S. L. Sessions, A. H. Sobel, and Ž. Fuchs, 2009: The mechanics of gross moist stability. *J. Adv. Model. Earth Syst.*, **1** (3), https://doi.org/10.3894/JAMES.2009.1.9.

Revadekar, J. V., H. Varikoden, P. K. Murumkar, and S. A. Ahmed, 2018: Latitudinal variation in summer monsoon rainfall over Western Ghat of India and its association with global sea surface temperatures. *Sci. Total Environ.*, **613–614**, 88–97, https://doi.org/10.1016/j.scitotenv.2017.08.285.

Robe, F. R., and K. A. Emanuel, 2001: The effect of vertical wind shear on radiative–convective equilibrium states. *J. Atmos. Sci.*, **58**, 1427–1445, https://doi.org/10.1175/1520-0469(2001)058<1427:TEOVWS>2.0.CO;2.

Robertson, A. W., V. Moron, J.-H. Qian, C.-P. Chang, F. Tangang, E. Aldrian, T. Y. Koh, and J. Liew, 2011: The Maritime Continent monsoon. *The Global Monsoon System: Research and Forecast*, 2nd ed., World Scientific, 85–98, https://doi.org/10.1142/9789814343411_0006.

Roe, G. H., 2005: Orographic precipitation. *Annu. Rev. Earth Planet. Sci.*, **33**, 645–671, https://doi.org/10.1146/annurev.earth.33.092203.122541.

Sawyer, J. S., 1956: The physical and dynamical problems of orographic rain. *Weather*, **11**, 375–381, https://doi.org/10.1002/j.1477-8696.1956.tb00264.x.

Seto, S., T. Iguchi, R. Meneghini, J. Awaka, T. Kubota, T. Masaki, and N. Takahashi, 2021: The precipitation rate retrieval algorithms for the GPM dual-frequency precipitation radar. *J. Meteor. Soc. Japan*, **99**, 205–237, https://doi.org/10.2151/jmsj.2021-011.

Shige, S., and C. D. Kummerow, 2016: Precipitation-top heights of heavy orographic rainfall in the Asian monsoon region. *J. Atmos. Sci.*, **73**, 3009–3024, https://doi.org/10.1175/JAS-D-15-0271.1.

——, Y. Nakano, and M. K. Yamamoto, 2017: Role of orography, diurnal cycle, and intraseasonal oscillation in summer monsoon rainfall over the Western Ghats and Myanmar Coast. *J. Climate*, **30**, 9365–9381, https://doi.org/10.1175/JCLI-D-16-0858.1.

Shrestha, D., R. Deshar, and K. Nakamura, 2015: Characteristics of summer precipitation around the Western Ghats and the Myanmar West Coast. *Int. J. Atmos. Sci.*, **2015**, 206016, https://doi.org/10.1155/2015/206016.

Sijikumar, S., L. John, and K. Manjusha, 2013: Sensitivity study on the role of Western Ghats in simulating the Asian summer monsoon characteristics. *Meteor. Atmos. Phys.*, **120**, 53–60, https://doi.org/10.1007/s00703-013-0238-8.

Sikka, D. R., 1977: Some aspects of the life history, structure and movement of monsoon depressions. *Pure Appl. Geophys.*, **115**, 1501–1529, https://doi.org/10.1007/BF00874421.

Smith, I., A. Moise, K. Inape, B. Murphy, R. Colman, S. Power, and C. Chung, 2013: ENSO-related rainfall changes over the New Guinea region. *J. Geophys. Res. Atmos.*, **118**, 10 665–10 675, https://doi.org/10.1002/jgrd.50818.

Smith, R. B., 1979: The influence of mountains on the atmosphere. *Adv. Geophys.*, **21**, 87–230, https://doi.org/10.1016/S0065-2687(08)60262-9.

——, 1989: Hydrostatic airflow over mountains. *Adv. Geophys.*, **31**, 1–41, https://doi.org/10.1016/S0065-2687(08)60052-7.

——, 2019: 100 years of progress on mountain meteorology research. *A Century of Progress in Atmospheric and Related Sciences: Celebrating the American Meteorological Society Centennial*, *Meteor. Monogr.*, No. 59, Amer. Meteor. Soc., https://doi.org/10.1175/AMSMONOGRAPHS-D-18-0022.1.

——, and Y.-L. Lin, 1983: Orographic rain on the Western Ghats. *Proceedings of the First Sino-American Workshop on Mountain Meteorology*, E. R. Reiter, Q. Yongfu, and Z. Baozhen, Eds., Science Press, 71–94.

——, and I. Barstad, 2004: A linear theory of orographic precipitation. *J. Atmos. Sci.*, **61**, 1377–1391, https://doi.org/10.1175/1520-0469(2004)061<1377:ALTOOP>2.0.CO;2.

Sobel, A. H., J. Nilsson, and L. M. Polvani, 2001: The weak temperature gradient approximation and balanced tropical moisture waves. *J. Atmos. Sci.*, **58**, 3650–3665, https://doi.org/10.1175/1520-0469(2001)058<3650:TWTGAA>2.0.CO;2.

——, C. D. Burleyson, and S. E. Yuter, 2011: Rain on small tropical islands. *J. Geophys. Res.*, **116**, D08102, https://doi.org/10.1029/2010JD014695.

Tawde, S. A., and C. Singh, 2015: Investigation of orographic features influencing spatial distribution of rainfall over the Western Ghats of India using satellite data. *Int. J. Climatol.*, **35**, 2280–2293, https://doi.org/10.1002/joc.4146.

Tropical Rainfall Measuring Mission, 2021: GPM PR on TRMM reflectivity, precipitation statistics, histograms, at surface and fixed heights, 1 month 5 × 5 and 0.25 × 0.25 degree V07. Goddard Earth Sciences Data and Information Services Center (GES DISC), accessed 10 September 2023, https://doi.org/10.5067/GPM/PR/TRMM/3A-MONTH/07.

Van den Hende, C., B. Van Schaeybroeck, J. Nyssen, S. Van Vooren, M. Van Ginderachter, and P. Termonia, 2021: Analysis of rainshadows in the Ethiopian Mountains using climatological model data. *Climate Dyn.*, **56**, 1663–1679, https://doi.org/10.1007/s00382-020-05554-2.

Viviroli, D., M. Kummu, M. Meybeck, M. Kallio, and Y. Wada, 2020: Increasing dependence of lowland populations on mountain water resources. *Nat. Sustainability*, **3**, 917–928, https://doi.org/10.1038/s41893-020-0559-9.

Wang, S., and A. H. Sobel, 2017: Factors controlling rain on small tropical islands: Diurnal cycle, large-scale wind speed, and topography. *J. Atmos. Sci.*, **74**, 3515–3532, https://doi.org/10.1175/JAS-D-16-0344.1.

Wilks, D. S., 2016: "The stippling shows statistically significant grid points": How research results are routinely overstated and overinterpreted, and what to do about it. *Bull. Amer. Meteor. Soc.*, **97**, 2263–2273, https://doi.org/10.1175/BAMS-D-15-00267.1.

Wu, C.-H., W.-R. Huang, and S.-Y. S. Wang, 2018: Role of Indochina Peninsula topography in precipitation seasonality over East Asia. *Atmosphere*, **9**, 255, https://doi.org/10.3390/atmos9070255.

Xie, S., T. Hume, C. Jakob, S. A. Klein, R. B. McCoy, and M. Zhang, 2010: Observed large-scale structures and diabatic heating and drying profiles during TWP-ICE. *J. Climate*, **23**, 57–79, https://doi.org/10.1175/2009JCLI3071.1.

Xie, S.-P., H. Xu, N. H. Saji, Y. Wang, and W. T. Liu, 2006: Role of narrow mountains in large-scale organization of Asian monsoon convection. *J. Climate*, **19**, 3420–3429, https://doi.org/10.1175/JCLI3777.1.

Yen, M.-C., T.-C. Chen, H.-L. Hu, R.-Y. Tzeng, D. T. Dinh, T. T. T. Nguyen, and C. J. Wong, 2011: Interannual variation of the fall rainfall in central Vietnam. *J. Meteor. Soc. Japan*, **89A**, 259–270, https://doi.org/10.2151/jmsj.2011-A16.

Zhang, G., and R. B. Smith, 2018: Numerical study of physical processes controlling summer precipitation over the Western Ghats region. *J. Climate*, **31**, 3099–3115, https://doi.org/10.1175/JCLI-D-17-0002.1.